https://doi.org/10.1038/s41593-024-01680-w

Spatiotemporally selective astrocytic ATP dynamics encode injury information sensed by microglia following brain injury in mice

Yue Chen[1,9], Pengwei Luan [1,2,9], Juan Liu [1,2,9], Yelan Wei[1,3], Chenyu Wang[1,4], Rui Wu[1,5], Zhaofa Wu [6,7,8] & Miao Jing [1]✉

Injuries to the brain result in tunable cell responses paired with stimulus properties, suggesting the existence of intrinsic processes that encode and transmit injury information; however, the molecular mechanism of injury information encoding is unclear. Here, using ATP fluorescent indicators, we identify injury-evoked spatiotemporally selective ATP dynamics, Inflares, in adult mice of both sexes. Inflares are actively released from astrocytes and act as the internal representations of injury. Inflares encode injury intensity and position at their population level through frequency changes and are further decoded by microglia, driving changes in their activation state. Mismatches between Inflares and injury severity lead to microglia dysfunction and worsening of injury outcome. Blocking Inflares in ischemic stroke in mice reduces secondary damage and improves recovery of function. Our results suggest that astrocytic ATP dynamics encode injury information and are sensed by microglia.

Living organisms require precise representations for diverse stimuli to survive, especially those that disrupt tissue homeostasis and affect fundamental functions. Injuries to the brain, either caused by external trauma or internal perturbations, represent major life-threating stimuli that directly cause or are accompanied with diseases[1,2]. The injury signaling was originally viewed to be passively transmitted, with the leakage of molecules from damaged cells, termed as damage-associated molecular patterns (DAMPs), which directly recruit local immune cells for management[3,4]; however, accumulating evidence supports that injury responses are precisely organized in time and space, and are tunable to match injury properties[5,6], including their types, severity and locations. This suggests the existence of active processes to encode and process injury information and guide corresponding responses. Unfortunately, the underlying cellular and molecular mechanism remains unclear.

The identification of internal injury representations is the prerequisite for mechanistic understanding. It has been shown that purinergic molecules, lipid mediators and chemokines could accumulate after injury and regulate microglia as the major effectors, suggesting that they may carry and present injury information[7–9]. Among them, ATP released from damaged cells has been extensively studied as an injury mediator[10,11]. Seminal work using bioluminescence imaging has reported the bulk increase of ATP surrounding the spinal cord injury, suggesting extracellular ATP as injury-responsive signals[12]. In cultured cells, application of ATP altered cytokine secretion and cellular behaviors of microglia[13,14]. Blocking ATP or its receptor P2Y$_{12}$R on microglia greatly attenuated injury response in vivo[15,16]; however, besides passive release, it is still unclear whether ATP can serve as an active signal to encode and process injury information and affect injury outcome. One

[1]Chinese Institute for Brain Research, Beijing, China. [2]Academy for Advanced Interdisciplinary Studies, Peking University, Beijing, China. [3]Department of College of Physical Education and Sport, Beijing Normal University, Beijing, China. [4]Capital Medical University, Basic Medical Sciences, Beijing, China. [5]China Agricultural University, Beijing, China. [6]State Key Laboratory of Membrane Biology, Peking University School of Life Sciences, Beijing, China. [7]PKU-IDG/McGovern Institute for Brain Research, Beijing, China. [8]State Key Laboratory of Molecular Developmental Biology, Institute of Genetics and Developmental Biology, Chinese Academy of Sciences, Beijing, China. [9]These authors contributed equally: Yue Chen, Pengwei Luan, Juan Liu. ✉e-mail: jingmiao@cibr.ac.cn
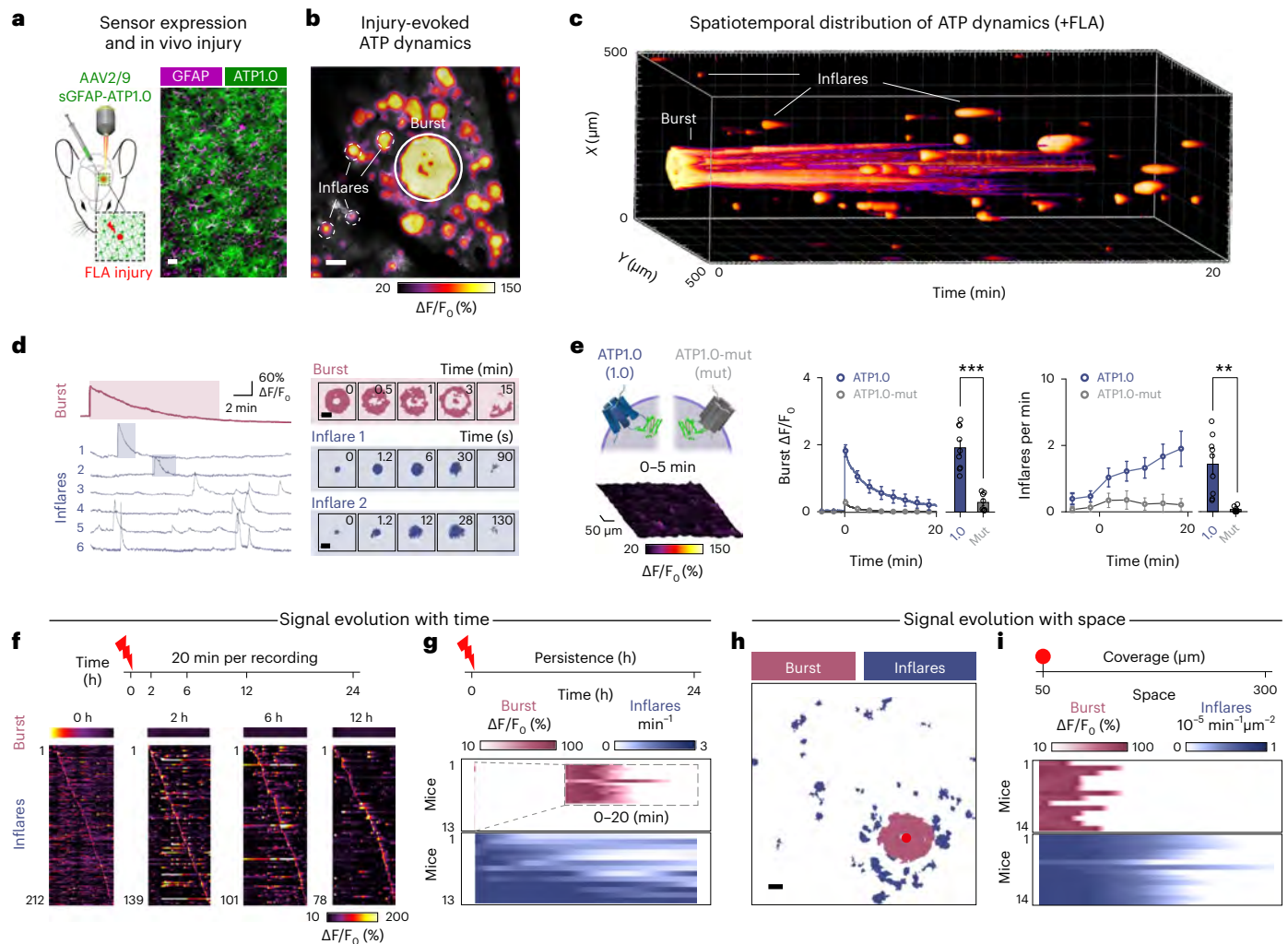
Fig. 1 | Spatiotemporally selective ATP events as internal injury representations. a, Schematic illustration of experiments, with AAV-sGFAP-ATP1.0 (sGFAP is also named as GfaABC1D) injection, two-photon imaging and FLA conducted in awake mice (left). Expression of ATP1.0 sensors (membrane localized, green) in astrocytes (GFAP, magenta) (right). **b**, Representative image of the ATP1.0 fluorescence responses after FLA, with signals over 20 min projected. The $\Delta F/F_0$ pseudocolor is overlaid on the raw fluorescence signal. The ATP burst (burst) and Inflares are labeled, respectively. **c**, The 3D-distribution of ATP dynamics after FLA in time and space. The x and y axes indicate the imaging field and the horizontal axis indicate time after FLA. **d**, Fluorescence traces of the ATP burst (magenta, up) and exemplar Inflares (blue, bottom) after FLA (left). Spatial progression of individual signals in shaded regions from traces, with the time after signal initiation labeled (right). **e**, Schematic illustration and group analysis of the ATP burst ($\Delta F/F_0$) and Inflare frequency in ATP1.0 (1.0, blue)

or ATP1.0-mut (Mut, gray) mice ($n = 9$ and 8 mice for 1.0 and Mut; $P = 1.9 \times 10^{-5}$ for burst, $P = 0.0016$ for Inflares). The representative fluorescence response of Mut-expressing mice (1–3 min after FLA) is shown for comparison. **f**, Representative traces (20 min) of the ATP burst (up) and Inflares (bottom) at indicated times after FLA. **g**, The persistence of ATP burst and Inflares after FLA, with each line representing signals from one mouse ($n = 13$ mice). The data for ATP burst are magnified on a different scale. **h**, Representative image showing the spatial distribution of ATP bursts and Inflares after injury, with the red dot indicating the position of FLA. **i**, Group analysis of the coverage of ATP burst and Inflares after FLA, with each line representing data from one mouse ($n = 14$ mice). Scale bars, 50 μm, except 10 μm for Inflares in **d**. Data are shown as mean ± s.e.m. **$P < 0.01$; ***$P < 0.001$. All statistical tests were two-sided (see Supplementary Table 1 for statistics).

limitation is the lack of methods to monitor ATP dynamics in vivo, with sufficient sensitivity and spatiotemporal resolution[17].

In our recent study, we developed genetically encoded fluorescent sensors GRAB$_{ATP1.0}$ (ATP1.0) for sensitive monitoring of ATP dynamics in vivo[18]. Equipped with this tool, here we precisely tracked the injury-evoked ATP in awake mice at sub-second resolution and identified spatiotemporally selective ATP events, named Inflares (INjury-induced FLAshing ATP RElease), which acted as an internal representation of injury. Inflares were actively released from astrocytes and could encode multiple aspects of injury information by their population properties, which was subsequently decoded by microglia to drive their behavioral changes. We further revealed that Inflares were universal representations in injury-related diseases, and blocking

excessive Inflares could be a promising treatment for ischemic stroke. Our work provides evidence that injury information could be actively sensed and transmitted and identified the underlying mechanism in injury signal processing.

Results

Microglia can sense injury indirectly

We first investigated whether there is a functional requirement for active injury encoding. To quantitatively assess injury and the internal response, we established the focal laser ablation (FLA) model[15,19] to precisely introduce injury in vivo, and simultaneously conducted two-photon imaging of microglia as an indication of injury response (Extended Data Fig. 1a,b). Notably, we observed a sharp difference in

spatiotemporal properties between the injury and microglial response. The local (50 μm in diameter) and brief (2 s) laser injury was able to recruit microglia from a broad area (>300 μm) sustainably for hours, analyzed both at a population and single-cell level (Extended Data Fig. 1c–j). The spatiotemporal differences between injury and microglial behavior suggest that microglia may require the internal representations that encode and process injury information.

Spatiotemporally selective ATP as injury representations

To image ATP dynamics as a potential injury representation, we virally expressed ATP1.0 sensors on astrocytes and monitored extracellular ATP level during FLA in mice (Fig. 1a, both female and male). Before FLA (−FLA), the sensor fluorescence remained stable with only a few local fluctuations. Immediately following FLA (+FLA), two distinct types of events were recorded, one was a bulk increase surrounding the injury center (ATP burst) and the other appeared as scattered, flashing-like signals across entire field of view (Fig. 1b–d and Supplementary Video 1). We named each individual flashing event as an Inflare. Sensors expressed in either neurons or astrocytes were able to detect both extracellular ATP events (Extended Data Fig. 2a–e).

To validate the signal represented ATP dynamics, we utilized the ATP1.0-mutant sensors (ATP1.0-mut) that cannot bind ATP but share the same protein backbone[18]. In ATP1.0-mut-expressing mice, FLA injuries failed to elicit detectable fluorescence response (Fig. 1e). Also, there was no correlation between fluorescence changes and basal fluorescence level of ATP1.0, suggesting that signals were not caused by heterogeneous sensor expression (Extended Data Fig. 2f–h). Collectively, the recording of injury-specific ATP dynamics implies that they might serve as injury representations.

Population Inflares are persistent and widespread

Injury representation needs to bridge the spatiotemporal gap between injury and microglial response. We thus compared the spatiotemporal properties of ATP burst and Inflares at both the single event and group levels. Quantification revealed that the ATP burst and Inflares could be distinguished based on single event properties, with the ATP burst exhibiting a stronger response ($\Delta F/F_0$), larger area and longer duration than a single Inflare (Extended Data Fig. 2i,j). Single Inflares were homogenously independent of the time and position of their occurrence (Extended Data Fig. 3a–f), suggesting that they function as fundamental signaling units.

Next, we analyzed the evolution of ATP dynamics after injury. The ATP burst occurred uniquely and diminished within 20 min, whereas Inflares were repeatedly generated (4–5 events per min in 2,500 μm²) for nearly 24 h (Fig. 1f). With an enlarged field of view, we further revealed that the ATP burst was concentrated around the injury, whereas Inflares were individually isolated but widespread in space. For a quantitative comparison, we defined the time of effective signal presentation (higher than baseline) as signal persistence and the maximum distance of effective signal over injury as signal coverage. The persistence of total Inflares (~20.8 h) was over 100-fold longer than that of the ATP burst (~0.17 h) (Fig. 1g) and the coverage of Inflares (~180 μm) was over twofold greater than that of the ATP burst (~70 μm) (Fig. 1h,i). We conclude that Inflares are capable of transmitting information to the microglia in persistent and widespread patterns.

Inflares encode injury intensity by frequency modulation

Injury representation can potentially encode information at either the individual or population level (Fig. 2a). To explore how Inflares encode injury intensity, we generated three degrees of injuries and recorded Inflares correspondingly. The spatial and temporal properties of Inflares were plotted separately for quantitative comparison (Fig. 2b). Across different injuries, single Inflares exhibited all-or-none properties, with no differences in the distribution of amplitude, size and duration, suggesting that the information was not encoded at the

single-event level (Fig. 2c,d,f,g). In contrast, the frequency of Inflares was positively correlated with the gain-of-injury intensity (Fig. 2e,h) and could be used for signal segregation between injuries (Fig. 2i). Multiple Inflares could also be generated at a single-cell level, indicating that such frequency modulation might involve regulation in cellular activities (Extended Data Fig. 3g–i). In sum, Inflares translate injury intensity by frequency modulation, with the single event remaining constant, reminiscent of rate coding in neuronal action potentials[20].

We further trained a multiple linear regression model by inputting paired injury information and Inflare properties, to see whether we could retrospectively predict injuries from Inflares (Fig. 2j). The properties of Inflares were inputted as predictors, with tunable weights to match the injury intensity as outputs. The successfully trained model predicted injury intensity with high accuracy, outperforming models using shuffled data (Fig. 2k). In the well-predicting model, population frequency ranked as the top contributor, whereas the properties of individual Inflares showed negligible contributions, consistent with the coding strategy (Extended Data Fig. 3j,k). Excluding the Inflare frequency from inputs or shuffling the pairing between frequency and injury both resulted in models with poor predictive power (Extended Data Fig. 3l). The quantitative relationship further suggests that Inflares are able to encode injury information.

Gradient distribution of Inflares encode injury position

An important feature of the internal injury response is the directional migration of microglia[21]. As a single Inflare is short-lived, we reason that Inflares might also encode positional information at the population level. Indeed, when Inflares were projected over time, we observed a gradient decrease of Inflare density with increasing distance to the injury (Fig. 3a). Such a gradient spanned a broad region (>300 μm) and could maintain directionality for hours (Fig. 3b–d and Extended Data Fig. 4a–c). As a signal gradient is a better reflection of relative but not absolute value, we examined whether changing the Inflare number altered the gradient properties. Analyzing Inflares in weak or medium injuries revealed similar spatial gradients in slope and coverage, although the absolute number of Inflares differed by tenfold (Fig. 3e). When switching FLA injuries to different locations, the location of Inflare gradients perfectly followed the injury center, while the intrinsic shape of the gradients remained constant (Fig. 3f). We extracted the Inflare gradient center and aligned it with the sites of FLA, and defined a successful spatial encoding when the gradient center fell within the damaged region (mismatch <100 μm). The FLA-evoked Inflare gradient showed a high accuracy with a 90% success encoding rate, in contrast to the failure of spatial encoding by Inflares before FLA or by randomly distributed events with a similar frequency (Extended Data Fig. 4d,e).

We next examined the minimal time required for Inflares to generate a robust gradient, with the mismatch distance between the gradient center and injury as the index. We found that temporal integration of Inflares for less than 5 min was enough to establish an accurate gradient (Extended Data Fig. 4f), reflecting the efficiency of Inflares in encoding spatial information.

In addition to location, we also explored whether Inflares could encode other spatial properties of injury. Changing the aspect ratio of the injury resulted in a corresponding alteration of the Inflare gradient, despite the fact that absolute ratios were not exactly the same due to gradient overlapping. Similarly, the deflection angle (to the horizontal line) of the Inflare gradient also matched that of injury (Extended Data Fig. 4g,h). In summary, the gradient distribution of Inflares faithfully and comprehensively encode the spatial information of injury.

Inflares are released from astrocytes through pannexin 1

Given the importance of Inflare as a representation of internal injury, we next explored the underlying cellular and molecular mechanisms. We first checked whether Inflares represented passive ATP release due to the breakage of membrane integrity. The necrosis cell marker
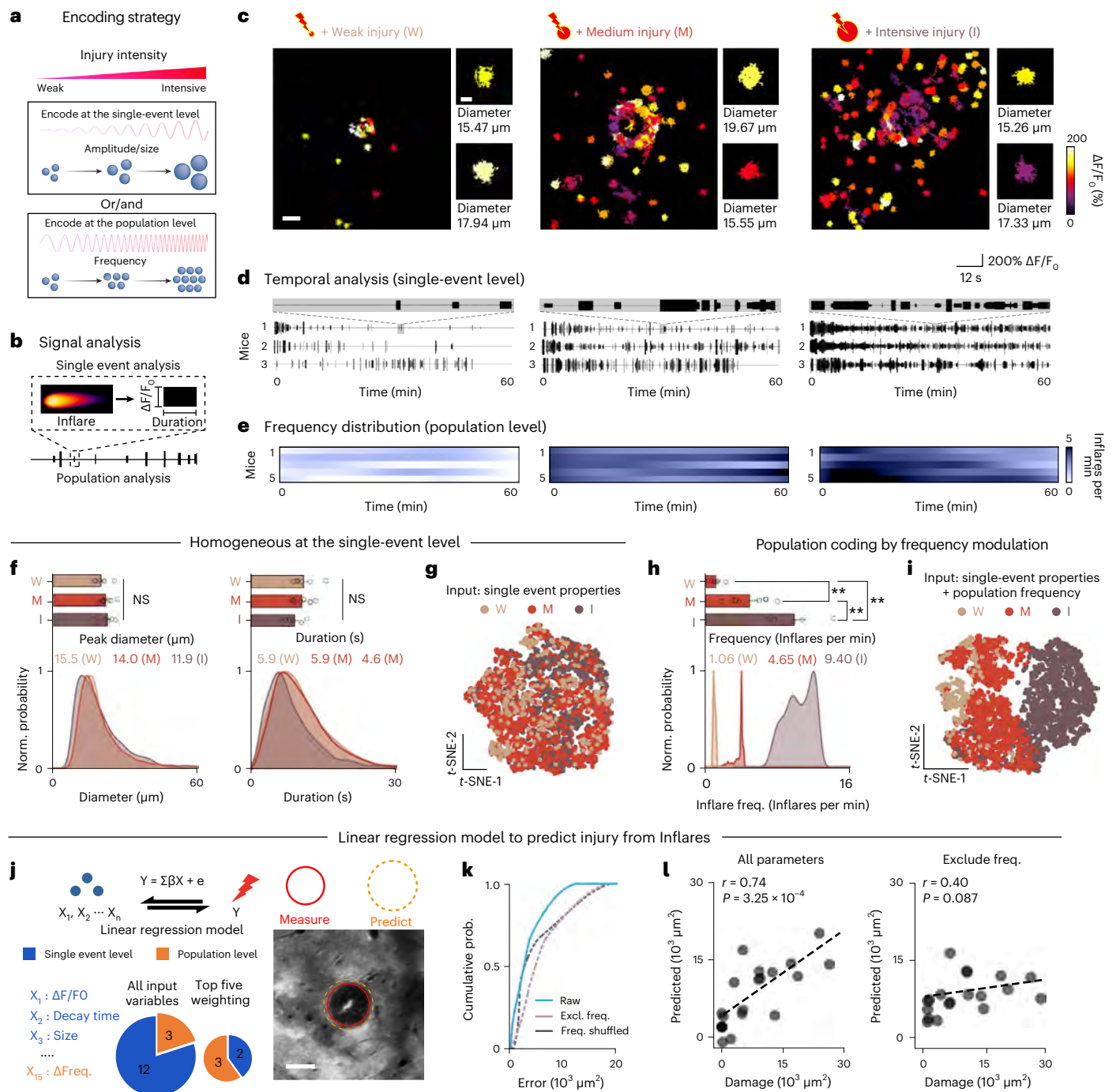
Fig. 2 | Inflares encode injury intensity by frequency modulation.
a, Illustration of potential encoding strategies by changes of individual Inflares (single-event level) or by changes in the Inflare frequency (population level) or both. **b**, Illustration of signal analysis of Inflare properties. **c**, Inflares (over 20 min) evoked by weak (W; left), medium (M; middle) or intensive (I; right) FLA injuries. Two typical Inflares in each group are zoomed in with their diameters labeled. **d**, The temporal analysis of individual Inflares after FLA, with the shaded area magnified ($n = 3$ mice). **e**, The frequency of Inflares at different times after FLA ($n = 5$ mice). **f**, The comparison of Inflare diameter (left) and duration (left) in different injuries ($n = 6$, 8 and 5 mice for W, M and I, respectively). **g**, The dimensional reduction of Inflares in all groups by t-distributed stochastic neighbor embedding. The individual properties of Inflares ($\Delta F/F_0$, duration, rise time, decay time, size and peak time) are used as input ($n = 5,435$ Inflares). **h**, The comparison of Inflare population frequencies in different injuries ($n = 6$,

8 and 5 mice for W, M and I; $P = 0.0015$ between W and M; $P = 0.0018$ between W and I; and $P = 0.0046$ between M and I). **i**, Similar to **g**, except that the population frequency was added for dimensional reduction. **j**, Predicting injury intensity using a linear regression model. A total of 15 independent parameters are used (see Extended Data Fig. 3k). The comparison of damage size (red) and Inflare-predicted damage (orange) is shown (right). **k**, The cumulative probability distribution of prediction error in models using raw data (raw), data with Inflare frequency shuffled (Freq. shuffled) or data that exclude frequency from inputs (Excl. freq.). **l**, The correlation analysis of Inflare-predicted damage with applied damage, using all Inflare parameters (left) or excluding Inflare frequency (right). Scale bars, 50 μm, except 10 μm for magnified Inflares in **c**. Data are shown as mean ± s.e.m. **$P < 0.01$; ***$P < 0.001$; NS, not significant. All statistical tests were two-sided (see Supplementary Table 1 for statistics).
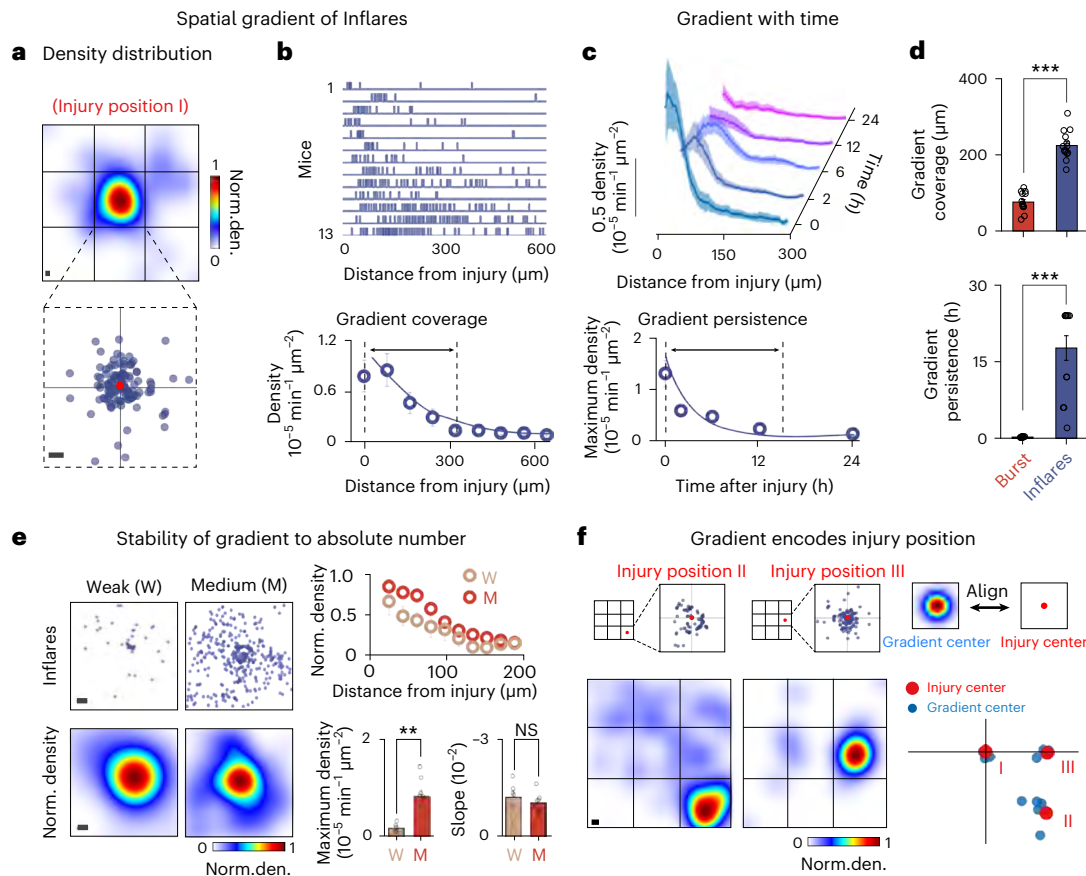
Fig. 3 | Gradient distribution of Inflares encodes injury position and shape. a, The spatial distribution of FLA-evoked Inflares (5 min after FLA). Kernel density distribution of Inflares (top). Raw data showing the Inflare regions of interests (ROIs) (bottom). **b,** Group analysis of the Inflare gradient distribution after injury, with Inflares shown as bars and each line representing data from one mouse ($n = 13$ mice). The change of Inflare density over distance is summarized below, with the gradient coverage indicated as the maximum distance of signal distribution above baseline. **c,** Changes of Inflare gradients at the indicated time points after FLA. The changes of maximum Inflare density over time are summarized below, with the gradient persistence indicated as the signal duration above baseline. **d,** Group analysis of the gradient coverage (up) and persistence (bottom) of ATP bursts and Inflares ($n = 9$ mice for coverage; $n = 13$ mice for persistence). The detailed analysis of the ATP burst is summarized in Extended Data Fig. 4a–c. **e,** The comparison of Inflare gradients evoked by different FLA intensities. **f,** Representative images of Inflare gradients that followed with changes of FLA locations (left). Alignment of Inflare gradient center (blue) with the FLA center applied (red) ($n = 14$ mice) (right). Detailed statistics are summarized in Extended Data Fig. 4d,e. Scale bars, 50 μm. Data are shown as mean ± s.e.m. **$P < 0.01$; ***$P < 0.001$; NS, not significant. All statistical tests are two-sided (see Supplementary Table 1 for statistics).

propidium iodide (PI) was injected before injury and FLA-evoked Inflares were recorded in the PI-labeling area (Fig. 4a). We observed no colocalization between PI signals and Inflares, whereas PI could clearly label dead cells that were directly exposed to the laser (Fig. 4b). Moreover, there was no time-dependent increase of PI labeling after FLA (Fig. 4c,d). Also, we did not observe any structural or fluorescence changes following Inflares (Fig. 4e), validating that Inflares are not due to passive ATP release from dying cells.

To uncover cellular mediators, we first conducted cell-type-specific perturbations to locally ablate or silence specific cell types and checked FLA-evoked Inflares under such backgrounds in vivo. Sufficient surgical recovery was performed to minimize the direct effect caused by cell ablation and no notable elevation of Inflares before FLA was recorded (Fig. 4f). Selective ablation of local astrocytes was achieved by either gliotoxin injection (L-α-aminoadipate (L-αAA); -Ast. I)[22] or genetically through the thymidine kinase system (AAV-sGFAP-HSV-TK + GCV injection; -Ast. II)[23] and validated by immunofluorescence (Extended Data Fig. 5a–e). With astrocytes ablated, FLA failed to evoke an elevation of Inflares (Fig. 4f and Extended Data Fig. 5c,f). As controls, mice received either artificial cerebrospinal fluid (ACSF) injection (for L-αAA) or GCV alone (without HSV-TK); all showed robust FLA-evoked Inflares. Ablation of neurons by caspase-3 expression (AAV-hSyn-taCasp3)[24]

or silencing neural activity by chemogenetics (AAV-hSyn-hM4Di + clozapine N-oxide (CNO)) did not affect subsequent FLA-evoked Inflares (Fig. 4g and Extended Data Fig. 5g–l). FLA-evoked Inflares were also recorded when the microglia were depleted by the CSF1R inhibitor, BLZ945 (ref. 25) (Fig. 4h and Extended Data Fig. 5m–o). Although each cell-type ablation might influence the integrated cellular network, combining these results showed that astrocytes are the potential cellular contributor for injury-evoked Inflares.

To explore whether Inflares require an elevation of astrocytic Ca^{2+}, we first imaged the Ca^{2+} dynamics using the red Ca^{2+} sensor jRGECO1a[26]. Immediately after FLA, a continuous Ca^{2+} wave was recorded within astrocytes, which originated from the injury center and rapidly propagated across the entire field (Fig. 4i and Extended Data Fig. 6a,b). The Ca^{2+} wave propagated faster and covered a larger area than the ATP burst and was insensitive to the application of ATP hydrolase (apyrase) or ATP receptor antagonists (PPADS + suramin)[27], while being constrained by gap-junction blockers[28] (Extended Data Fig. 6b–f). We further explored the causal relationship between astrocytic Ca^{2+} and Inflares. Depleting the intracellular Ca^{2+} store, either by the SERCA inhibitor thapsigargin (TG)[29] or by astrocytic expression of the Ca^{2+} pump hPMCA2w/b[30], abolished the increase in Inflares (Fig. 4j,k). Blocking gap junctions decreased the coverage of Inflares (Extended Data

Fig. 6g–h), implying that Inflare-generating astrocytes were interconnected within a functional domain. To test the sufficiency of Ca^{2+}, we elevated astrocytic Ca^{2+} using a chemogenetic approach in the absence of injury[31] (Extended Data Fig. 6i). CNO application successfully triggered Ca^{2+} transients and elevated Inflares in hM_3Dq-expressing astrocytes (Fig. 4l and Extended Data Fig. 6j). Chemogenetically activated astrocytes shared a similar status to those after injury, as further introducing FLA in the presence of CNO failed to evoke an additional increase in Inflares (Extended Data Fig. 6k,l). Detailed analysis revealed that Inflares were not always accompanied by local Ca^{2+} transients (Extended Data Fig. 6n–p), suggesting that sustained Inflare regeneration may depend on the downstream signals of Ca^{2+}.

To explore the molecular mediators of Inflares, we selected candidates that are involved in ATP release[32–34] and are highly expressed in astrocytes[35]. We individually applied blockers of these candidates in brain slices to screen their effects on FLA-evoked Inflares. Multiple blockers of the pannexin 1 hemichannel, including probenecid (PBN)[36], trovafloxacin (TROVA)[37] and the peptide inhibitor [10]Panx1 (ref. 38) were all effective in blocking FLA-induced Inflares, whereas the scrambled peptide (scPanx1) and inhibitors for other candidates were not (Fig. 4m). We further validated screening results through a series of genetic manipulations. Knock down of $Panx1$ by shRNA diminished the FLA-evoked Inflares in vivo (Extended Data Fig. 7a–c). Astrocyte-specific $Panx1$ knockout ($Panx1^{flox/flox}$ crossed with $GFAP$-$creERT2$) abolished the FLA-evoked increase of Inflares, whereas neuronal $Panx1$ knockout did not (Fig. 4n). Similar results were obtained using Cas9-dependent $Panx1$ knockout (Extended Data Fig. 7a,d,e). Conversely, overexpressing Panx1 proteins in astrocytes significantly boosted FLA-evoked Inflares (Fig. 4o). Of note, all the above-mentioned pharmacological and genetic perturbations selectively affected Inflares, whereas neither the ATP burst nor the astrocytic Ca^{2+} wave was altered (Extended Data Fig. 7f–i). The cell-specific changes of Panx1 proteins were validated by immunostaining (Extended Data Fig. 7j–m). Genetic manipulation of astrocytic $Panx1$ also shifted the correct injury encoding (Fig. 4p), implying that dysfunction within astrocytes may lead to mismatched information transmission.

Microglia decode information from Inflares

Inflares, as the representation of injury, encode injury information and match the spatiotemporal response of microglia; however, it is unclear whether microglia decode injury from Inflares. We first tested whether persistent Inflares are required to drive microglial changes (Fig. 5a). Compared with ACSF injection, injecting the apyrase after the initiation of FLA dramatically decreased the persistence of Inflares and led to the inhibition of microglial accumulation (Fig. 5b–d). We excluded other factors that may affect microglia, including differences in injuries and microglial states or the enzymatic activity-independent effects of apyrase[39] (Extended Data Fig. 8a–e). Critically, at a temporal scale, we found a positive linear relationship between Inflares and changes in microglial migration (Δmigration) (Fig. 5e). Microglial processes were also able to sense local Inflares and performed directional extension (Extended Data Fig. 8f,g). This suggests that microglia are able to continuously decode Inflare information and adjust their performance.

Next, we evaluated the injury-decoding properties of microglia with Inflares manipulated. In astrocytic $Panx1$ conditional knockout mice (cKO) where Inflares were blocked, the directional microglia response was totally inhibited, even with the same FLA applied. Conversely, boosting Inflares by overexpressing (OE) astrocytic Panx1 led to elevated microglial accumulation (Fig. 5f). Notably, regardless of changes in Inflares, the quantitative relationship between Inflares and microglia remained constant, while tuning Inflares shifted the pairing between initial injury and microglia (Fig. 5g,h, red dashed lines indicate the relationship without $Panx1$ manipulation). These results show that microglia can faithfully decode injury information carried by Inflares.

As microglial responses are critical for injury management, we next tested how information processing affects the outcome of injury. At 24 h after FLA, an increase in cell apoptosis was observed, which served as an indicator for injury consequence. In astrocytic $Panx1$ cKO mice, FLA-induced cell apoptosis was greatly attenuated. Oppositely, elevating Inflares through Panx1 OE exacerbated cellular apoptosis after FLA (Fig. 5i). Analysis of signal relationships revealed that the injury outcome matched well with Inflares, but poorly with the initial injury, consistent with the above result for microglia (Fig. 5j,k).

To test whether changes of injury outcome were microglia-dependent, we systematically analyzed the properties of microglia after injury and compared them in the presence or absence of Inflares. FLA induced the morphological transformation of microglia from typical branching to an ameboid-like shape, reflecting the transition of microglial state after injury. The presence of Inflares was necessary for driving such changes, with the blocker PBN or astrocytic $Panx1$ cKO reversed the FLA-induced change (Fig. 5l and Extended Data Fig. 8h,i). The FLA-induced increase of microglial proliferation was also blocked by the elimination of Inflares (Fig. 5m). We also accessed the functional changes of microglia after injury, including their phagocytosis and transcriptional status, which all showed Inflare-dependent alterations to FLA (Fig. 5n and Extended Data Figs. 8j–l and 9a,b). Of note, the alteration of injury outcome required microglia as the downstream mediator, as microglia-depleted mice did not show Inflare-dependent changes in local cell apoptosis (Extended Data Fig. 9c–e). We conclude that Inflares broadly affect the state of microglia, resulting in their dysfunction, which contributes to the exacerbated injury outcome (Fig. 5o).

## Blocking excessive Inflares benefits stroke recovery

To check whether Inflares serve as a universal representation of injury, particularly in human disease-relevant contexts, we performed in vivo two-photon imaging of ATP dynamics in middle cerebral artery occlusion (MCAO) mice, which modeled ischemic stroke[40] (Fig. 6a,b and Supplementary Video 2). In the cortex of mice, Inflares could be observed in different stages of stroke progression (ischemia and reperfusion) with varying frequencies (Fig. 6c). In contrast, Inflares were rarely recorded in sham surgery mice or mice expressing the ATP1.0-mutant sensor that were subjected to MCAO (Fig. 6c). Astrocytic $Panx1$ cKO or PBN injection also resulted in no increase of Inflares during MCAO (Fig. 6d,e). Population Inflares were able to encode the injury severity, as Inflare frequency and tissue damage showed a linear correlation, supporting the encoding principle of Inflares (Fig. 6f,g).

Fig. 4 | Ca^{2+} and Panx1-dependent Inflares from astrocytes. a,b, Experimental design and Inflares in PI-injected mice. **c**, Relationship between PI intensity and $\Delta F/F_0$ of Inflares ($n = 385$ Inflares from three mice). **d**, PI intensities in Inflare ROIs across time ($n = 3$ mice). **e**, The fluorescence of ATP1.0 at baseline or after Inflares ($n = 385$ Inflares from three mice). **f**, Inflares (20 min, same in figures below) in vehicle or astrocytic ablated mice ($n = 6$, 6 and 7 mice for vehicle, -Ast. I and -Ast. II). **g**, Inflares in control, neuronal ablation (-Neu.) or inhibition (↓Neu.) mice ($n ≥ 4$ mice). **h**, Inflares in vehicle or microglia-depleted mice (-Mic.) ($n = 8$ and 9 mice for vehicle and -Mic.). **i**, FLA-evoked jRGECO1a signals in astrocytes in vivo. **j**, Changes of astrocytic Ca^{2+} and Inflares in artificial cerebrospinal fluid (ACSF) or TG-treated slices ($n = 5$ slices for curves; $n = 7$ slices from three mice for statistics) (left). **k**,

Inflares in astrocytic hPMCA2w/b or mCherry-expressing slices ($n = 5$ and 6 slices from two mice). **l**, Inflares in astrocytic hM_3Dq expressing or control ($-hM_3Dq$) slices to CNO application ($n = 7$ and 8 slices from 3 and 2 mice for $+hM_3Dq$ and $-hM_3Dq$). **m**, Inflare change to FLA in brain slices treated with indicated blockers ($n ≥ 7$ slices from ≥3 mice). **n**, Inflares in astrocytic ($n = 9$ mice) or neuronal $Panx1$ cKO mice ($n = 5$ mice). $Panx1^{flox/flox}$ mice were used as controls ($n = 3$ mice). **o**, Inflares in astrocytic mCherry or Panx1-overexpressing (OE) mice ($n = 5$ mice; $P = 0.0482$). **p**, Encoding of injury in mice with panx1 perturbations ($n = 9$, 9 and 5 mice for wild-type (WT), cKO and OE). Scale bars, 50 μm, except 10 μm for zoomed images in **b**. Data are shown as mean ± s.e.m. *, $p < 0.05$; **, $P < 0.01$; ***, $P < 0.001$; NS, not significant. All statistical tests were two-sided (see Supplementary Table 1 for statistics).

As Inflares cause microglia dysfunction and exacerbate cell apoptosis in FLA, we hypothesize that overwhelming Inflares in MCAO (tenfold higher than FLA) might cause excessive injury response, and blocking Inflares by targeting Panx1 might benefit stroke recovery. Panx1 blockage or astrocyte-specific cKO prevented pathological changes in gene transcripts after MCAO (Fig. 6h–j) and areas of brain
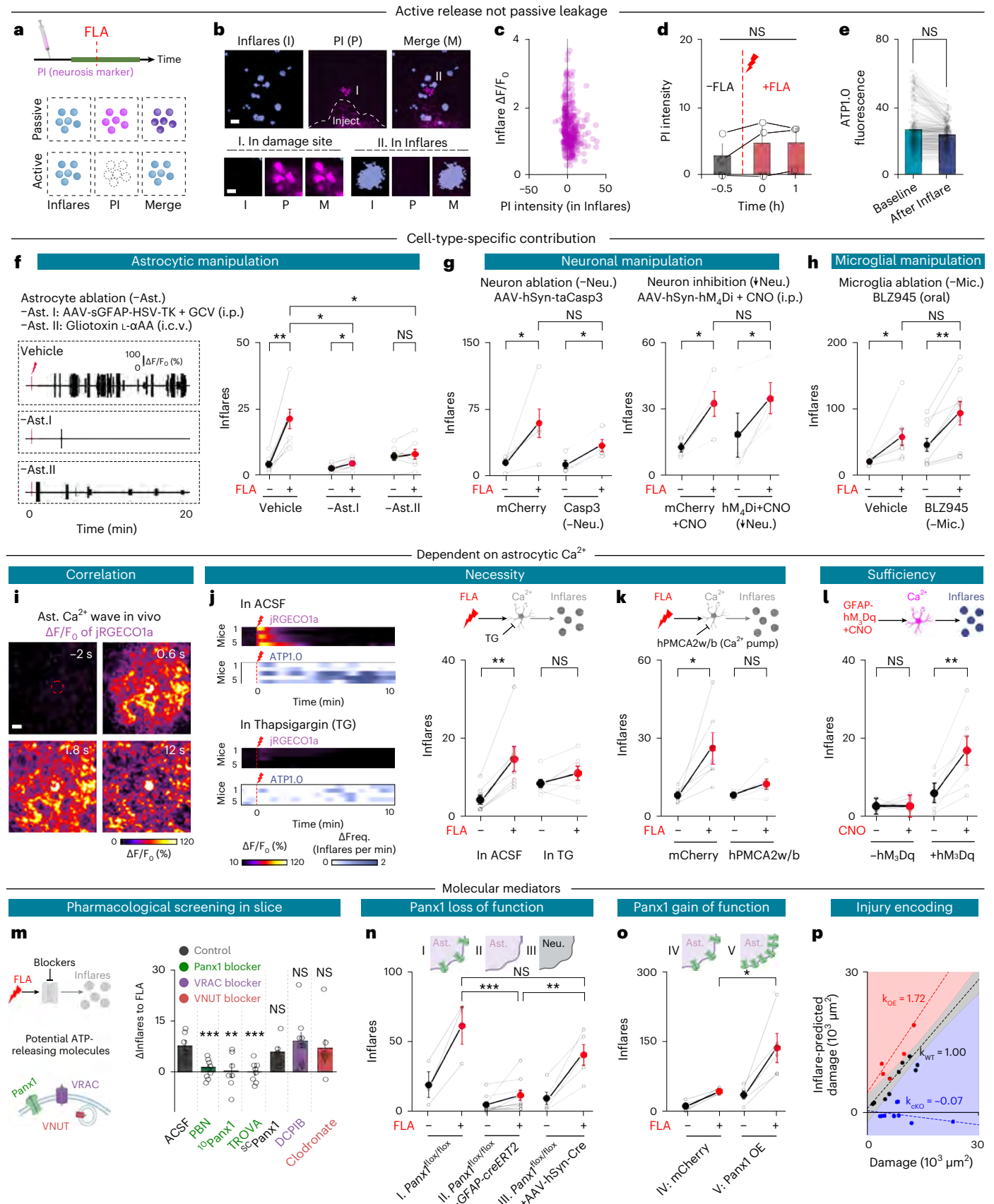
infarction were significantly reduced, especially in the penumbra region facing secondary injury (Fig. 6k and Extended Data Fig. 10a, b). Behaviorally, mice with Panx1 blockage or knockout recovered more effectively with minor abnormalities, including lower neurological deficit scores[41], stronger locomotion and balancing ability compared to saline-treated MCAO mice or with *Panx1*flox/flox mice as controls (Fig. 6l–n and Extended Data Fig. 10c–e). Although the inhibitor PBN might have multiple functional targets[42], combining the genetic evidence suggests that rationally blocking Inflares by targeting Panx1 represents a promising way to manage stroke-related brain injury.

Discussion

Information encoding and processing are essential for the coordinated function in biological systems[43,44]. Each system may utilize unique principles during signal transmission to match the diverse changes of external and internal states. Here, we report spatiotemporally selective Inflares as an internal representation of injury, which effectively encode multiple aspects of injury information within their properties, and further present information to initiate microglial response. We also reveal that the encoding principles of Inflares are fundamentally similar to that used in neurons, which may benefit signal transmission in the highly dynamic in vivo system and thus have been evolutionarily selected.

To understand how molecules encode information, it is critical to capture them with high sensitivity and spatiotemporal resolution. In fact, various information is processed in the dimensions of time and space, often together with amplitude to increase coding capacity[45,46]. Understanding the principle of information processing requires studies to be shifted from knowing the presence to precisely capturing the dynamics, which places great demand on technique innovations.

Before our work, the detailed characterization of ATP dynamics was hindered by the recording methods, and its releasing mode and regulatory mechanism in a biological context were not fully clear[47]. The intracellular concentration of ATP is typically ~10^6 times higher than the extracellular level[48], which provides a huge energy for ATP to flow out. Injuries that cause cell necrosis open the path for ATP by breaking membrane integrity, resulting in the leakage of ATP[49]. It has also been reported that cells receiving threatening challenges irreversibly cleaved the C terminus of Panx1 channels, leading to ATP release and apoptosis[50]. Therefore, ATP is currently documented as the 'find me' signal, classified into DAMPs that leak out from dead or dying cells to activate microglia[3]; however, some observations cannot be reconciled with this theory, implying a more complex regulation for ATP. As the extracellular ATP is rapidly degraded by richly expressing enzymes CD39 and CD73 (ref. 51), the half-life of ATP is at the second to minute level[52], providing a relative short time window that cannot match the timescale of microglial response. Furthermore, minor damage or even neuronal hyperactivity is able to recruit microglia in an ATP-dependent manner but without the presence of cell death[53]. Our identification of Inflares suggests that ATP release can be actively regulated depending on cellular activities, through which information can be precisely controlled and processed, rather than only being passively passed by as a consequence of injury. The involvement of astrocytic Inflares suggests that ATP may not only be viewed as a find me signal for dying cells, but also serves as a 'go there' (or come here) signal originating from the astrocyte network that monitors local perturbations. Nevertheless, our work did not exclude that ATP could be released from other cellular sources with a distinct molecular mechanism. Also, ATP Inflares could work synergistically with other molecules in the encoding and presentation of injury information, for example together with the well-documented DAMPs.

How does the spatiotemporal pattern of Inflares encode information? Through analyzing Inflares at individual and population levels, we uncover that Inflares encode injury intensity through frequency modulation, and at the same time, encode injury location through gradient distribution. By constructing a linear regression model, the accurate prediction of injury information retrospectively from Inflares further supports the encoding ability. Together, Inflares by their properties can encode the when, where and how (strength) of injuries, providing a comprehensive characterization. A follow-up question is on the who (or what) aspect, that is, whether Inflares can encode the identity of injuries. Notably, we recently reported a similar flashing pattern of ATP during lipopolysaccharide-induced systemic inflammation in vivo[18]. Further comparison of Inflares recorded under multiple stimuli might provide the answer.

Signal encoding is widely observed in the brain, which transforms both concrete and abstractive information into the brain's own language; however, most existing studies have focused on the contribution of neurons[54], whereas limited research touched on astrocytes[55]. One argument is that the major astrocytic signal, the intracellular Ca^{2+}, is analog and lacks enough coding sensitivity and capacity compared to the digitized action potentials of neurons[56]. Nevertheless, increasing evidence suggests that astrocytes may work in parallel or in coordination with neurons to encode selective information[57]. Our work demonstrated the involvement of astrocytes in injury coding and processing, which is not secondary or indirectly related to neurons. Of note, the digitized Inflares that we identified provide the unit to encode information with sufficient accuracy and complexity. Theoretically, information processing in astrocytes provides another layer of computation, and understanding the similarities and differences in astrocytic computation can aid in the global study of the brain as a coordinated network.

Inflares, as extracellular signaling molecules, also contributed to the orchestrated cooperation between glial cells to achieve complex regulation. In contrast to the previous notion that microglia directly sense and respond to injury[16], our results suggest the functional specialization and coordination between astrocytes and microglia, in which astrocytes sense the injury and encode it with Inflares, while microglia subsequently decode the information for injury management. As microglia are limited in number with isolated territories[58], their direct detection of injury may lead to missed signals with less sensitivity. In contrast, astrocytes that form a tight network[59] are more robust in detecting injury. Furthermore, signal amplification achieved by Inflares opens a prolonged time window, during which slow cellular

Fig. 5 | Microglia decode injury information from Inflares. a, Illustration of experiments to block total (II) or persistent Inflares (III) by apyrase (1,000 U ml⁻¹) (n = 10, 5 and 5 mice for Inflares; n = 10, 5 and 9 mice for microglia in I, II and III, respectively). **b,** The changes of Inflares (top) and microglia (bottom) after FLA (n = 10, 5 and 5 mice in I, II and III, respectively). **c,d,** Inflare persistence and microglial migration index (relative fluorescence within FLA region) in each condition (n = 10, 5 and 9 mice for I, II and III, respectively). **e,** The relationship between Inflares and changes in microglial migration index (Δmigration index) (n = 10 mice). **f,** Microglial accumulation 8 h after FLA, in WT, cKO or astrocytic Panx1 OE mice (n = 6 mice; P = 3.53 × 10⁻⁴ between WT and cKO; P = 8.54 × 10⁻⁴ between WT and OE). **g,h,** The relationship between Inflares (**g**) or initial injury (**h**) with microglial numbers after FLA (n = 6 mice). **i,** Apoptotic cells (cleaved caspase-3-positive, red) at 8 h after FLA in different groups (n = 5 mice). **j,k,** The relationship between Inflares (**j**) or initial injury (**k**) with apoptotic cell number after FLA (n = 5 mice). **l,** Microglial morphology in −FLA (gray), +FLA with saline (red), +FLA with PBN (green) or +FLA in cKO mice (blue) 8 h after injury. Each dot represents a single microglia (n = 30 cells from 5 mice). **m,** Microglial proliferation (pro.) in WT or cKO mice 48 h after FLA (n = 5 mice). **n,** Microglial phagocytosis (pha.) in WT or cKO mice 8 h after FLA (n = 5 mice). The phagocytosis index (Ph index) is the percentage of apoptotic cells engulfed by microglia. **o,** Inflare-mediated injury signal transmission between glial cells. Scale bars, 50 μm, except 120 μm in **f** (top right) and 10 μm in **i** (top right). Data are shown as mean ± s.e.m. *P < 0.05; **P < 0.01; ***P < 0.001; NS, not significant. All statistical tests were two-sided (see Supplementary Table 1 for statistics).

processes such as migration can occur. The widespread Inflares in space also recruit cells from a broader area to ensure the effective injury management. Therefore, the multicellular network provides an ideal solution to achieve both sensitivity and efficiency in injury response.

The heterogenous and highly dynamic states of microglia[60], on the other hand, also suggests the presence of injury encoding that is

necessary for such tunable changes. Also, growing evidence indicates that microglia are able to precisely adjust their states to different stimuli[61]. These highly organized and selective responses enable microglia to cope with various conditions, rather than using an active or not active strategy. An important feature in this process, unfortunately less understood, is how various stimuli are presented to microglia for
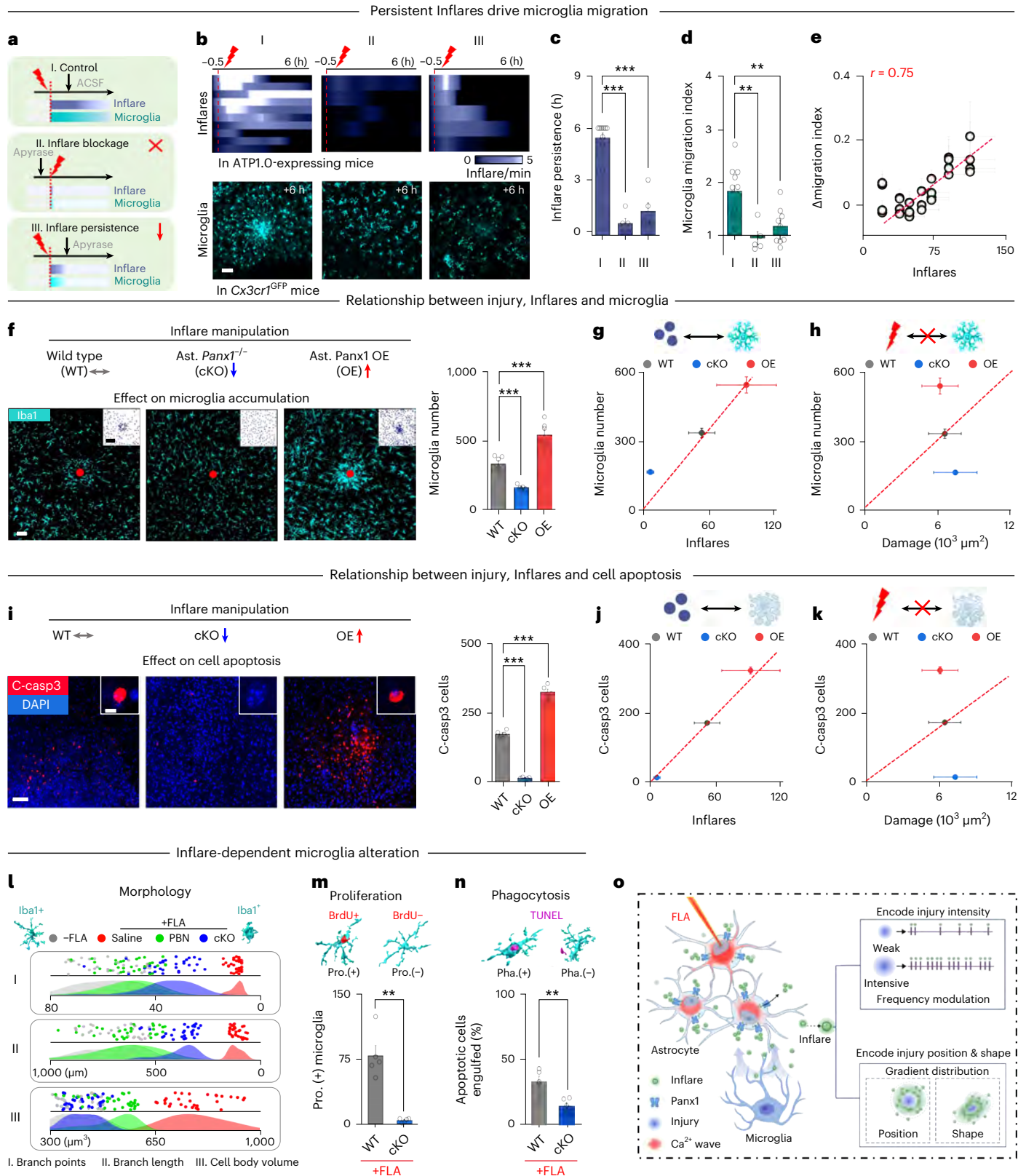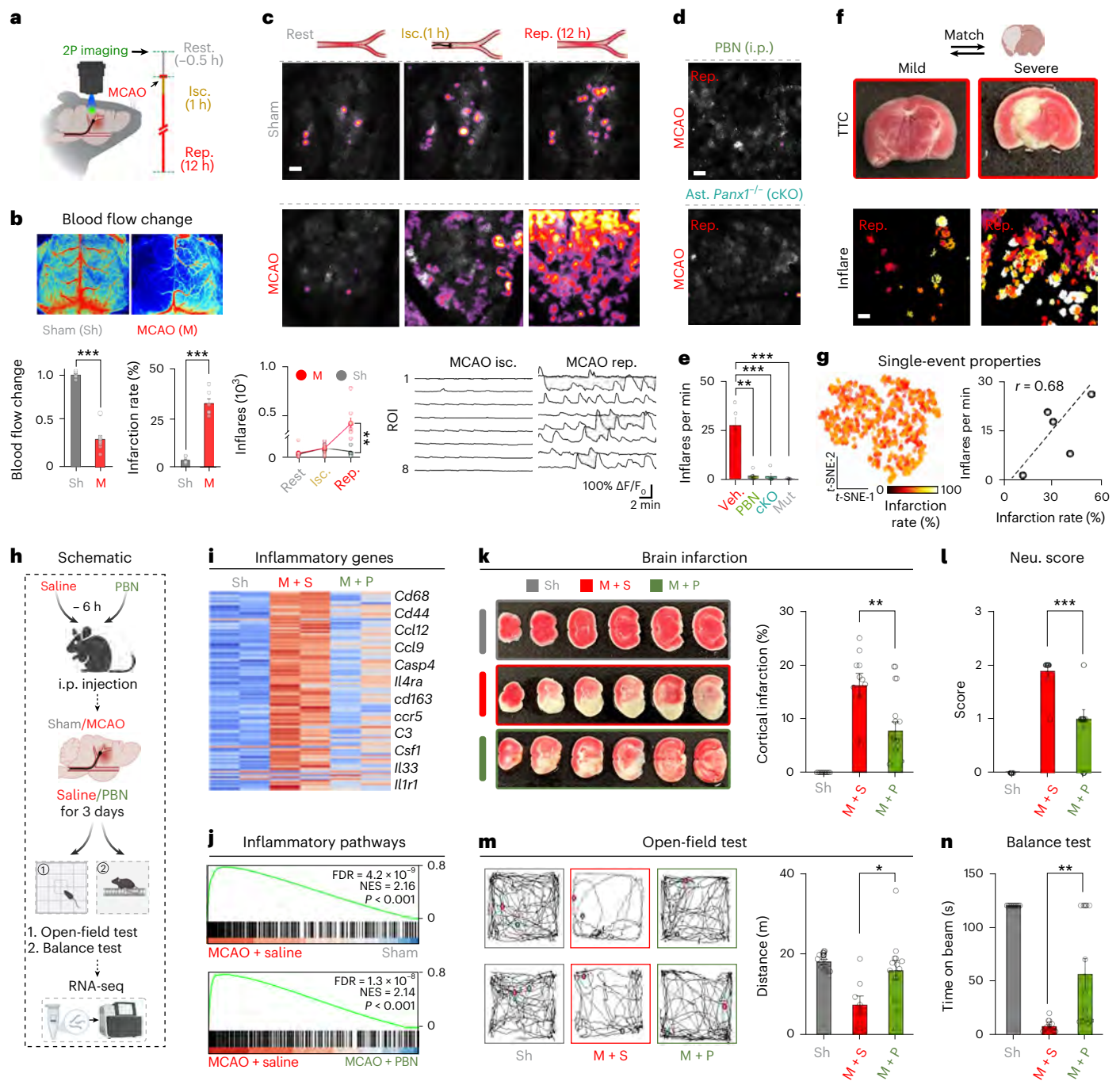
Fig. 6 | Blocking excessive Inflares in ischemic stroke benefits disease outcome. a, Illustration of the experimental setup. **b**, The changes in blood flow (n = 5 and 9 mice) and brain infarction rate (n = 6 mice) in sham (Sh) or MCAO mice (M). **c**, Inflares (over 10 min) at different states (resting, ischemia or reperfusion) in Sh and MCAO mice (n = 6 and 7 mice; P = 0.002). **d,e**, Inflares during reperfusion in MCAO mice with PBN (200 mg kg^{-1}, top), or in mice with astrocytic *Panx1* cKO (bottom) (n = 5, 4, 5 and 4 mice for MCAO, MCAO + PBN, cKO and MCAO (mut), respectively). **f**, The comparison of brain infarction and Inflares recorded. **g**, The relationship between single Inflare properties (left) or Inflare frequency (right) with MCAO infarction rate (n = 5 mice). **h**, Experimental design to check the function of Inflares. **i,j**, Expression of inflammatory genes

in Sh and MCAO mice injected with saline (M + S) and MCAO mice injected with PBN (M + P) (n = 2 mice). **k**, The brain infarction in different groups 3 days after surgery (P = 0.0062). **l**, The neurological-deficient scores in different groups after 3 days of surgery (n = 10, 9 and 12 mice for Sh, MCAO + saline, MCAO + PBN, respectively; P = 0.00081). **m**, The trajectory of mice in the open-field test (left). The total movement distance over 5 min (n = 10, 9 and 12 mice for Sh, MCAO + saline, MCAO + PBN, respectively; P = 0.027) (right). **n**, The total time of mice on the balance beam n = 10, 9 and 12 mice for Sh, MCAO + saline, MCAO + PBN, respectively; P = 0.0063). Scale bars, 50 μm. Data are shown as mean ± s.e.m. *P < 0.05; **P < 0.01; ***P < 0.001. All statistical tests were two-sided (see Supplementary Table 1 for statistics).

their selective changes. The characterization of Inflares that encode injury, as well as their profound effect on microglial behaviors, opens the possibility to further elucidate the decoding and computing strategy applied by microglia. For example, our data clearly exclude the

existence of a broad ATP concentration gradient that was originally thought to recruit microglia[14], and instead suggest that groups of isolated signals form a probabilistic gradient, whereby microglia may only encounter limited changes of ATP at certain times and positions.

We hypothesize that microglia may temporally integrate Inflares by intracellular signals or perform chemokinesis in response to individual Inflares during their migration.

The identification of internal injury representation updates the understanding of disease progression, and sheds light on the potential targets for treatments. As the injury outcome critically depends on the matched signal encoding and decoding, where any abnormal processing may result in an unpaired response and consequently, lead to insufficient or exacerbated injury management that become pathogenic. Keeping the balance for injury transmission, for example through targeting pannexin 1, might be an ideal way for future treatments on injury-related diseases.

Online content

Any methods, additional references, Nature Portfolio reporting summaries, source data, extended data, supplementary information, acknowledgements, peer review information; details of author contributions and competing interests; and statements of data and code availability are available at https://doi.org/10.1038/s41593-024-01680-w.

References

1. Feigin, V. L., Barker-Collo, S., Krishnamurthi, R., Theadom, A. & Starkey, N. Epidemiology of ischaemic stroke and traumatic brain injury. *Best. Pr. Res Clin. Anaesthesiol.* **24**, 485–494 (2010).
2. Ghajar, J. Traumatic brain injury. *Lancet* **356**, 923–929 (2000).
3. Liesz, A. et al. DAMP signaling is a key pathway inducing immune modulation after brain injury. *J. Neurosci.* **35**, 583–598 (2015).
4. Corps, K. N., Roth, T. L. & McGavern, D. B. Inflammation and neuroprotection in traumatic brain injury. *JAMA Neurol.* **72**, 355–362 (2015).
5. Loane, D. J. & Kumar, A. Microglia in the TBI brain: the good, the bad, and the dysregulated. *Exp. Neurol.* **275**, 316–327 (2016).
6. Gadani, S. P., Walsh, J. T., Lukens, J. R. & Kipnis, J. Dealing with danger in the CNS: the response of the immune system to injury. *Neuron* **87**, 47–62 (2015).
7. Di Virgilio, F., Sarti, A. C. & Coutinho-Silva, R. Purinergic signaling, DAMPs, and inflammation. *Am. J. Physiol. Cell Physiol.* **318**, C832–C835 (2020).
8. Mizuno, T., Kawanokuchi, J., Numata, K. & Suzumura, A. Production and neuroprotective functions of fractalkine in the central nervous system. *Brain Res.* **979**, 65–70 (2003).
9. Dewitt, D. S. et al. Experimental traumatic brain injury elevates brain prostaglandin E2 and thromboxane B2 levels in rats. *J. Neurotrauma* **5**, 303–313 (1988).
10. Malek Abrahimians, E., Carlier, V. A., Vander Elst, L. & Saint-Remy, J. M. MHC Class II-restricted epitopes containing an oxidoreductase activity prompt CD4(+) T cells with apoptosis-inducing properties. *Front. Immunol.* **6**, 449 (2015).
11. Bouras, M., Asehnoune, K. & Roquilly, A. Immune modulation after traumatic brain injury. *Front. Med.* **9**, 995044 (2022).
12. Wang, X. et al. P2X7 receptor inhibition improves recovery after spinal cord injury. *Nat. Med.* **10**, 821–827 (2004).
13. Ferrari, D. et al. Extracellular ATP triggers IL-1β release by activating the purinergic P2Z receptor of human macrophages. *J. Immunol.* **159**, 1451–1458 (1997).
14. Honda, S. et al. Extracellular ATP or ADP induce chemotaxis of cultured microglia through Gi/o-coupled P2Y receptors. *J. Neurosci.* **21**, 1975–1982 (2001).
15. Davalos, D. et al. ATP mediates rapid microglial response to local brain injury in vivo. *Nat. Neurosci.* **8**, 752–758 (2005).
16. Haynes, S. E. et al. The P2Y12 receptor regulates microglial activation by extracellular nucleotides. *Nat. Neurosci.* **9**, 1512–1519 (2006).
17. Wu, Z. & Li, Y. New frontiers in probing the dynamics of purinergic transmitters in vivo. *Neurosci. Res.* **152**, 35–43 (2020).
18. Wu, Z. et al. A sensitive GRAB sensor for detecting extracellular ATP in vitro and in vivo. *Neuron* **110**, 770–782 (2022).
19. Galbraith, J. A. & Terasaki, M. Controlled damage in thick specimens by multiphoton excitation. *Mol. Biol. Cell* **14**, 1808–1817 (2003).
20. Adrian, E. D. The impulses produced by sensory nerve-endings: part 4. Impulses from pain receptors. *J. Physiol.* **62**, 33–51 (1926).
21. Ahn, S. J., Anrather, J., Nishimura, N. & Schaffer, C. B. Diverse inflammatory response after cerebral microbleeds includes coordinated microglial migration and proliferation. *Stroke* **49**, 1719–1726 (2018).
22. Khurgel, M., Koo, A. C. & Ivy, G. O. Selective ablation of astrocytes by intracerebral injections of α-aminoadipate. *Glia* **16**, 351–358 (1996).
23. Delaney, C. L., Brenner, M. & Messing, A. Conditional ablation of cerebellar astrocytes in postnatal transgenic mice. *J. Neurosci.* **16**, 6908–6918 (1996).
24. Yang, C. F. et al. Sexually dimorphic neurons in the ventromedial hypothalamus govern mating in both sexes and aggression in males. *Cell* **153**, 896–909 (2013).
25. Hagemeyer, N. et al. Microglia contribute to normal myelinogenesis and to oligodendrocyte progenitor maintenance during adulthood. *Acta Neuropathol.* **134**, 441–458 (2017).
26. Dana, H. et al. Sensitive red protein calcium indicators for imaging neural activity. *eLife* **5**, e12727 (2016).
27. Charlton, S. J. et al. PPADS and suramin as antagonists at cloned P2Y- and P2U-purinoceptors. *Br. J. Pharmacol.* **118**, 704–710 (1996).
28. Saez, J. C., Retamal, M. A., Basilio, D., Bukauskas, F. F. & Bennett, M. V. Connexin-based gap junction hemichannels: gating mechanisms. *Biochim. Biophys. Acta* **1711**, 215–224 (2005).
29. Sehgal, P. et al. Inhibition of the sarco/endoplasmic reticulum (ER) Ca(2+)-ATPase by thapsigargin analogs induces cell death via ER Ca(2+) depletion and the unfolded protein response. *J. Biol. Chem.* **292**, 19656–19673 (2017).
30. Yu, X. et al. Reducing astrocyte calcium signaling in vivo alters striatal microcircuits and causes repetitive behavior. *Neuron* **99**, 1170–1187 (2018).
31. Agulhon, C. et al. Modulation of the autonomic nervous system and behaviour by acute glial cell Gq protein-coupled receptor activation in vivo. *J. Physiol.* **591**, 5599–5609 (2013).
32. Hyzinski-Garcia, M. C., Rudkouskaya, A. & Mongin, A. A. LRRC8A protein is indispensable for swelling-activated and ATP-induced release of excitatory amino acids in rat astrocytes. *J. Physiol.* **592**, 4855–4862 (2014).
33. Iglesias, R., Dahl, G., Qiu, F., Spray, D. C. & Scemes, E. Pannexin 1: the molecular substrate of astrocyte 'hemichannels'. *J. Neurosci.* **29**, 7092–7097 (2009).
34. Oya, M. et al. Vesicular nucleotide transporter is involved in ATP storage of secretory lysosomes in astrocytes. *Biochem. Biophys. Res. Commun.* **438**, 145–151 (2013).
35. Chai, H. et al. Neural circuit-specialized astrocytes: transcriptomic, proteomic, morphological, and functional evidence. *Neuron* **95**, 531–549 (2017).
36. Silverman, W., Locovei, S. & Dahl, G. Probenecid, a gout remedy, inhibits pannexin 1 channels. *Am. J. Physiol. Cell Physiol.* **295**, C761–C767 (2008).
37. Poon, I. K. et al. Unexpected link between an antibiotic, pannexin channels and apoptosis. *Nature* **507**, 329–334 (2014).
38. Brough, D., Pelegrin, P. & Rothwell, N. J. Pannexin-1-dependent caspase-1 activation and secretion of IL-1β is regulated by zinc. *Eur. J. Immunol.* **39**, 352–358 (2009).
39. Madry, C. et al. Effects of the ecto-ATPase apyrase on microglial ramification and surveillance reflect cell depolarization, not ATP depletion. *Proc. Natl Acad. Sci. USA* **115**, E1608–E1617 (2018).

40. Howells, D. W. et al. Different strokes for different folks: the rich diversity of animal models of focal cerebral ischemia. *J. Cereb. Blood Flow. Metab.* **30**, 1412–1431 (2010).

41. Schaar, K. L., Brenneman, M. M. & Savitz, S. I. Functional assessments in the rodent stroke model. *Exp. Transl. Stroke Med.* **2**, 13 (2010).

42. Garcia-Rodriguez, C. et al. Probenecid, an old drug with potential new uses for central nervous system disorders and neuroinflammation. *Biomedicines* **11**, 1516 (2023).

43. Purvis, J. E. & Lahav, G. Encoding and decoding cellular information through signaling dynamics. *Cell* **152**, 945–956 (2013).

44. Rolls, E. T. & Treves, A. The neuronal encoding of information in the brain. *Prog. Neurobiol.* **95**, 448–490 (2011).

45. Gurdon, J. B. & Bourillot, P. Y. Morphogen gradient interpretation. *Nature* **413**, 797–803 (2001).

46. Parodi, O., Combe, P. & Ducom, J. C. Temporal coding in vision: coding by the spike arrival times leads to oscillations in the case of moving targets. *Biol. Cybern.* **74**, 497–509 (1996).

47. Dosch, M., Gerber, J., Jebbawi, F. & Beldi, G. Mechanisms of ATP release by inflammatory cells. *Int. J. Mol. Sci.* **19**, 1222 (2018).

48. Ekstrand, M. et al. Depletion of ATP and glucose in advanced human atherosclerotic plaques. *PLoS ONE* **12**, e0178877 (2017).

49. Iyer, S. S. et al. Necrotic cells trigger a sterile inflammatory response through the Nlrp3 inflammasome. *Proc. Natl Acad. Sci. USA* **106**, 20388–20393 (2009).

50. Chekeni, F. B. et al. Pannexin 1 channels mediate 'find-me' signal release and membrane permeability during apoptosis. *Nature* **467**, 863–867 (2010).

51. Zimmermann, H. Biochemistry, localization and functional roles of ecto-nucleotidases in the nervous system. *Prog. Neurobiol.* **49**, 589–618 (1996).

52. Fitz, J. G. Regulation of cellular ATP release. *Trans. Am. Clin. Climatol. Assoc.* **118**, 199–208 (2007).

53. Eyo, U. B. et al. Neuronal hyperactivity recruits microglial processes via neuronal NMDA receptors and microglial P2Y12 receptors after status epilepticus. *J. Neurosci.* **34**, 10528–10540 (2014).

54. Borst, A. & Theunissen, F. E. Information theory and neural coding. *Nat. Neurosci.* **2**, 947–957 (1999).

55. Doron, A. et al. Hippocampal astrocytes encode reward location. *Nature* **609**, 772–778 (2022).

56. Smith, S. J. Do astrocytes process neural information? *Prog. Brain Res* **94**, 119–136 (1992).

57. Lines, J., Martin, E. D., Kofuji, P., Aguilar, J. & Araque, A. Astrocytes modulate sensory-evoked neuronal network activity. *Nat. Commun.* **11**, 3689 (2020).

58. Kettenmann, H., Hanisch, U. K., Noda, M. & Verkhratsky, A. Physiology of microglia. *Physiol. Rev.* **91**, 461–553 (2011).

59. Giaume, C. & McCarthy, K. D. Control of gap-junctional communication in astrocytic networks. *Trends Neurosci.* **19**, 319–325 (1996).

60. Hammond, T. R. et al. Single-Cell RNA sequencing of microglia throughout the mouse lifespan and in the injured brain reveals complex cell-state changes. *Immunity* **50**, 253–271 (2019).

61. Paolicelli, R. C. et al. Microglia states and nomenclature: a field at its crossroads. *Neuron* **110**, 3458–3483 (2022).

Methods

Animals

All animal surgery and procedures were performed according to protocols approved by the Animal Care and Use Committees of the Chinese Institute for Brain Research (CIBR) (CIBR-IACUC 007). Both female and male mice aged 5–7 weeks were used for in vivo surgery and two-photon imaging, while mice aged 5–7 days were employed for acute brain slices experiments. C57BL6/J mice (The Jackson Laboratory, IMSR JAX, 000664) were bred in the animal facility at CIBR. *Panx1* cKO mice (*Panx1*$^{flox/+}$, GemPharmatech, strain no. T008074) with 140 bp deletion in exon 2 were purchased from GemPharmatech. The LSL-Cas9-IRES-tdtomato transgenic mice (GemPharmatech, strain no. T002249) were generated by GemPharmatech and kindly provided by Y. Li's laboratory at Peking University. *GFAP-creERT2* mice (MMRRC, stock 016992-MU) were originally obtained from MMRRC and were kindly provided by W. Ge's laboratory at CIBR. The astrocytic *Panx1* knockout mice was achieved by crossing *Panx1*$^{flox/flox}$ mice with *GFAP-creERT2* mice. *Cx3cr1*$^{GFP/+}$ mice (The Jackson Laboratory, IMSR JAX: 005582) were originally purchased from The Jackson Laboratory. All mice were either family-housed or pair-housed in a temperature-controlled room with a 12-h light–dark cycle. Animals were randomly assigned to treatment groups, and experiments and analyses were performed blinded to treatment assignments. No statistical methods were used to predetermine sample size and sample sizes are indicated for each experiment and were chosen based on similar previous studies[62,63].

Viruses

AAV-sGFAP-mCherry (WZ Bioscience, AV200088), AAV2/9-hSyn-mCherry (WZ Bioscience, AV200068), AAV2/9-sGFAP (GfaABC1D)-hM$_3$D (Gq)-mCherry (WZ Bioscience, AV202006), AAV2/9-hSyn-hM4D (Gi)-mCherry (WZ Bioscience, AV202009) and AAV2/9-sGFAP-cre (WZ Bioscience, AV204012) were purchased from WZ Bioscience. AAV2/9-sGFAP-ATP1.0, AAV2/9-sGFAP-ATP1.0-mut, AAV2/9-sGFAP-jRGECO1a, AAV2/9-hSyn-taCaspase3, AAV2/9-hSyn-ATP1.0, AAV-sGFAP-mRuby3, AAV2/9-hSyn-cre, AAV2/9-sGFAP-HSV-TK-mCherry, AAV2/9-hPMCA2w/b-mCherry, AAV2/9-sGFAP-cre-gRNA-Panx1, AAV2/9-U6-Panx1-shRNA-scramble, AAV-PHP.eB-sGFAP-cre, AAV-PHP.eB-mCherry and AAV-sGFAP-Panx1 were packaged from the vector core at CIBR. All adeno-associated viruses (AAVs) were aliquoted and stored at −80 °C until use.

The following oligonucleotides were used in this study:
Panx1-sgRNA-1 (F-CACCGCCACTTCAAGTACCCAATCG and R-AAACCGATTGGGTACTTGAAGTGGC);
Panx1-sgRNA-2 (F-CACCGGAAGAACGTGTAGACGACCA and R-AAACTGGTCGTCTACACGTTCTTCC);
Panx1-sgRNA-3 (F-CACCGGTCCGAGAACACATACTCCG and R-AAACCGGAGTATGTGTTCTCGGACC);
Scrambled-sgRNA (F-CACCGGGTATTACTGATATTGGTGGG and R-AAACCCCACCAATATCAGTAATACCC);
Panx1-shRNA (GTGGACAAGATGGTCACATGT); scrambled shRNA (GCATGCCTACGCTTGTTCATT).

Stereotaxic surgery and virus injection

Mice were anesthetized with an intraperitoneal (i.p.) injection of avertin (250 mg kg^{-1}, Sigma-Aldrich, T48402) and a head-fixed recording chamber was affixed to the skull. After 3–4 days of recovery, mice were re-anesthetized and placed on a stereotaxic frame (RWD Instruments). A cranial window was opened on the visual cortex, followed by the injection of 400–500 nl AAV (coordinates of AP, −2.2 mm relative to Bregma; ML, 2.0 mm; and DV, 0.5 mm below the dura, with an angle of 30°) using a microsyringe pump (Nanoliter 2000 injector, WPI) at a rate of 30 nl min^{-1}. For an enlarged field of view image, AAVs were injected at three different positions (each 300 nl). After injection, the glass electrode was left for 5 min before slowly withdrawing. After cleaning with sterile saline, a coverslip was used to replace the skull.

Mice recovered from anesthesia under a heat pad. The *Cx3cr1*$^{GFP/+}$ mice underwent a similar surgery without AAV injection and recovered for 1 week before imaging. The *Panx1*$^{flox/flox}$ mice were orbitally injected with PHP.eB serotype AAV (50 μl per mouse) and expressed for 4 weeks. For acute brain slice experiments, P5–7 mice were anesthetized on a pre-cooled metal block and injected with 300 nl AAV into the visual cortex. Tissue glue was used to close the skin and mice were returned to their home cage after fully recovering from anesthesia.

Acute brain slice preparation

To prepare acute brain slices, mice were anesthetized after expression and were transcardially perfused with 5 ml pre-cooled slicing buffer containing 110 mM choline-Cl, 2.5 mM KCl, 1.25 mM NaH$_2$PO$_4$, 25 mM NaHCO$_3$, 25 mM glucose, 7 mM MgCl$_2$ and 0.5 mM CaCl$_2$. The brains were immediately removed and placed in pre-cooled oxygenated slicing buffer (with 95% O$_2$ + 5% CO$_2$). The brains were sectioned into 300-μm slices using a VT1200 vibratome (Leica) and slices containing the visual cortex were transferred to oxygenated ACSF containing 125 mM NaCl, 2.5 mM KCl, 1.25 mM NaH$_2$PO$_4$, 25 mM NaHCO$_3$, 25 mM glucose, 1.3 mM MgCl$_2$ and 2 mM CaCl$_2$. Slices were recovered at 33 °C for 30 min before being transferred to an imaging chamber.

Two-photon imaging and focal laser ablation

Imaging of awake mice and acute brain slices was conducted using a two-photon laser-scanning microscope (FVMPE-RS; Olympus). Images were acquired using a ×25 water immersion objective (XLPL-N25XWMP2, 1.05 NA, Olympus). For imaging ATP dynamics using GRAB-ATP1.0 sensors[15], the recording frequency was set at 10 Hz and every ten images were averaged. Each recording episode typically lasted for 20 min in vivo and 10 min for acute slices. For imaging microglia migration, z-stacks of images were captured with a 20-μm thickness using a 5-μm step size.

For generating FLA, the 920-nm laser was set at its maximum power and scanned the center of the imaging region (50 μm in diameter) for 2 s using the Tornado scanning mode. Successful FLA could be observed by the formation of a high fluorescence circle around the FLA region. For generating FLA with different intensities, the laser power and duration was adjusted (weak, 40% laser power for 0.4 s; medium, 100% laser power for 2 s; intensive, 100% laser power for 10 s). In slice experiments, the FLA protocol was set as 80% laser power for 1 s. In experiments related to microglia morphology, gene expression profiling and biochemical experiments, an extended FLA was performed in which a region of ~500 μm in diameter was injured to assess the injury outcome at the tissue level.

Cell-type-specific ablation and silencing

For astrocytic ablation, the HSV-TK substrate ganciclovir (MCE, HY-13637A) was i.p. injected at 100 mg kg^{-1} body weight for 14 consecutive days in mice expressing HSV-TK. The gliotoxin L-αAA (Aladdin, A100535, 500 nl) was prepared in ACSF at 20 mg ml^{-1} and locally injected near the sensor-expressing region. For neuronal ablation, AAV2/9-hSyn-taCaspase3 was expressed for 3 weeks. For neuron silencing, AAV2/9-hSyn-hM4Di-mCherry was expressed for 3 weeks and CNO (APExBIO, A3317, 10 mg kg^{-1}) was i.p. injected 30 min before imaging. For microglia ablation, the CSF1R inhibitor BLZ945 (MCE, HY-12768) was added to the food pellet at a concentration of 2 g kg^{-1} and mice were fed twice daily with 3 g of the palate for 21 consecutive days.

Drug administration

The detailed applications of drugs for in vivo experiments are listed as follows. Apyrase (1,000 U ml^{-1}, Sigma-Aldrich, A6237-100UN) was prepared in ACSF and locally injected 0.6 μl into the cortex near the imaging area. The apyrase was inactivated by heating at 90 °C for 40 min before injection. The hM$_4$Di synthetic ligand CNO (250 μM) was dissolved in saline and i.p. administered (300 μl). Pannexin blocker PBN

(4 mg ml^{-1}, Invitrogen, P36400) was also administered at 200 mg kg^{-1}, 40 min before in vivo imaging or FLA stimulation. PI (Beyotime, ST512) was locally injected (5 mg ml^{-1}) into the imaging area, 30 min before recording. 5-Bromodeoxyuridine (BrdU) (250 mg kg^{-1}, Beyotime, ST1056-500mg) was i.p. injected 30 min before FLA. To induce cre recombinase expression in *GFAP-creERT2* transgenic mice, tamoxifen (Sigma-Aldrich, T5648) was added to the food pellet at a concentration of 500 mg kg^{-1} and *GFAP-creERT2* mice were given the food every day for 21 consecutive days.

The detailed application of drugs in the acute slice experiments was as follows: TG (10 µM, MCE, HY-13433) was bath-applied for 40 min before imaging. Other drugs including CNO (10 µM), pyridoxalphosphate-6-azophenyl-2′,4′-disulphonic acid (PPADS; 100 µM, TOCRIS, 0625), suramin (100 µM, Sigma-Aldrich, S2671), carbenoxolone (CBX; 100 µM, MCE, HY-B1367), 1-octanol (100 µM, MCE, HY-W032013), PBN (1 mM), TROVA (50 µM, MCE, HY-A0170), ^{10}Panx1 (100 µM, Sigma-Aldrich, SML2152), ^{sc}Panx1 (100 µM, Sigma-Aldrich, SML2082), DCPIB (20 µM, R&D, 1540/10) and clodronate (10 µM, MCE, HY-107794) were all bath-applied in the imaging chamber for 5 min before imaging.

Histology

Mice brains were dissected after FLA, with −FLA samples from contralateral areas that did not receive FLA. Mice were anesthetized and transcardially perfused with saline, following 4% paraformaldehyde (PFA) in phosphate-buffered saline (PBS). The brains were post-fixed in 4% PFA at 4 °C overnight and then transferred to 30% sucrose/PBS at 4 °C for 48–72 h. Brains were sectioned on a freezing microtome (Leica, CM3050S) and coronal sections (50 µm) of the visual cortex were collected.

For immunofluorescence (IF), sections were permeabilized with 0.5% Triton X-100 (Sigma-Aldrich, 9036-19-5) in PBS, blocked with 5% BSA at room temperature for 1 h and incubated with primary antibodies (1:1,000, except rabbit anti-pannexin 1 at 1:200) in a humidified chamber at 4 °C overnight. The sections were stained with secondary antibodies (1:1,000) at room temperature for 2 h, mounted with 4,6-diamidino-2-phenylindole (Sigma-Aldrich, D9542) in glycerol/PBS (0.1 µg ml^{-1}) on coverslips.

The following primary antibodies were used in this study: rabbit anti-Iba1 (Abcam, ab178846); chicken anti-GFAP (Abcam, ab4674); rabbit anti-GFAP (Abcam, ab7260); rabbit anti-NeuN (Abcam, ab177487); mouse anti-NeuN (Abcam, ab104224); rabbit anti-GFP (Abcam, ab290), rat anti-BrdU (Abcam, ab6326); rat anti-CD68 (Abcam, ab53444); rabbit anti-cleaved caspase-3 (Cell Signaling Technology, 9661); rabbit anti-pannxin1 (Thermo Fisher Scientific, 488100); rabbit anti-caspase-3 (Cell Signaling Technology, 9662); and mouse anti-β-actin (Abcam, ab8226). Secondary antibodies included: Alexa Fluor 488 goat anti-rabbit IgG (Abcam, ab150077); Alexa Fluor 555 goat anti-rabbit IgG (Abcam, ab150078); Alexa Fluor 488 goat anti-mouse IgG H&L (Abcam, ab150113); Alexa Fluor 555 goat anti-mouse IgG (Abcam, ab150114); Alexa Fluor 647 goat anti-chicken IgY (Abcam, ab150171); Alexa Fluor 647 goat anti-rat IgG H&L (Abcam, ab150167); horseradish peroxidase (HRP)-conjugated rabbit anti-mouse IgG H&L (Abcam, ab6728); and HRP-conjugated goat anti-rabbit IgG H&L (MultiSciences, GAR0072)

For proliferation experiments, an antigen-retrieval step for BrdU detection was performed with 2 M HCl for 30 min at 37 °C, followed by incubation with 0.1 M, pH 8.5, sodium borate for 10 min before common immunostaining. Apoptosis cells were detected using terminal deoxynucleotidyl transferase dUTP nick end labeling (TUNEL) assay following the manufacturer's instructions, using the One Step TUNEL Apoptosis Assay kit (Beyotime, C1090).

Z-stack images (50 µm) of IF samples were obtained using a laser-scanning confocal microscope (Leica TCS SP8) and analyzed with Imaris software (Oxford Instruments, v.9.70).

For western blotting analysis, brain cortex tissues were isolated

at 8 h after FLA and homogenized on ice in RIPA lysis buffer (Beyotime, P0013B) supplemented with protease inhibitor cocktail (Thermo Scientific, 78429). Then, 50 µg total proteins were loaded and separated by SDS−PAGE and transferred onto PVDF membranes. The membranes were blocked with 5% BSA in TBS containing 0.1% Tween-20 and incubated with primary antibodies, including rabbit anti-cleaved caspase-3 (Asp175) (1:1,000 dilution), rabbit anti-caspase-3 (1:1,000 dilution) and mouse anti-β-actin (1:1,000 dilution) at 4 °C overnight. HRP-conjugated goat anti-rabbit IgG H&L (1:5,000 dilution) and HRP-conjugated rabbit anti-mouse IgG H&L (1:1,000 dilution) were used as secondary antibodies at room temperature for 1 h. Signals were detected using Super ECL Detection Reagent by Invitrogen Chemiluminescent Imaging System (Invitrogen). The bands were quantified using ImageJ (1.53q) software (National Institutes of Health).

Gene expression profiling

For quantitative real-time PCR analysis (qPCR), total RNA was extracted from the cortex. The concentration and purity of RNA were evaluated using a Nanodrop One spectrophotometer. Reverse transcription of cDNA and quantitative PCR was carried out using SYBR Green SuperMix (Transgene biotech, AQ601-03) on Real-Time PCR Detection System (Bio-Rad, CFX96). The relative mRNA expression level was calculated using the $2^{-\Delta\Delta CT}$ method. Each real-time PCR reaction was performed in triplicate. Primers for all genes were designed crossing exon−intron junctions. *β-actin* was used as an internal control.

Primer sequences were as follows:
Il1b (F-AATGCCACCTTTTGACAGTGAT and R-GATGTGCTGCT GCGAGATTT);
Il6 (F-ACTTCACAAGTCGGAGGCTT and R-GCCACTCCTTCTG TGACTCC);
Tnfa (F-CCCTCACACTCACAAACCAC and R-ATAGCAAATCG GCTGACGGT);
Ccl2 (F-ACCTGCTGCTACTCATTCACC and R-ATTCCTTCTTGGGGT CAGCA);
Il10 (F-GGTTGCCAAGCCTTATCGGA and R-CACCTTGGTCTTGGA GCTTATT);
β-actin (F-GCGGGCGACGATGCT and R-TCATCTTTTCACGGTT GGCCT).

For bulk RNA sequencing, brain samples were dissected and the extracted RNA and send to Novogene (Beijing) for subsequent steps. A total of 1 µg RNA per sample was used as input material. Then, following the manufacturer's protocols, we collected purified mRNA, synthesized cDNA and second-strand cDNA and constructed the cDNA library. After cluster generation, the library preparations were sequenced on an Illumina Novaseq platform, generating 150-bp paired-end reads.

MCAO model

Male C57BL/6J mice aged 4–6 weeks and weighing 20–25 g were used in the study[64,65]. In brief, mice were anesthetized and the common carotid artery, internal carotid artery and external carotid artery were separated. A 6-0 nylon suture coated with silica gel was inserted through the external carotid artery, followed by the internal carotid artery and gently inserted into the middle cerebral artery to induce MCAO. The success of occlusion was determined by monitoring the decrease in surface cerebral blood flow (CBF) to 30–40% of baseline CBF using a laser speckle instrument (SIM BFI WF). Reperfusion was performed by withdrawing the suture 1 h after MCAO. In imaging experiments, PBN (200 mg kg^{-1}) was administered via i.p. injection to the mouse before MCAO at two time points, 6 h before surgery and 6 h after reperfusion. In behavioral analysis, PBN was injected consecutively for 3 days at the same concentration.

TTC (2,3,5-triphenyltetrazolium chloride) staining was employed to assess brain damage after MCAO surgery. In detail, the brains were cut into six coronal slices (2-mm thickness). The slices were stained with 2% TTC (Sigma-Aldrich, T8877) for 10 min at 37 °C and fixed with

4% PFA for 5 min. Images of the stained sections were captured using a digital camera. The infarction area on each TTC-stained section was measured using ImageJ. The infarction rate (%) was calculated as (the area of viable brain tissue in the right hemisphere − the area of viable brain tissue in the left hemisphere) × 100/total area of the slice.

Behavioral analysis

The neurological score of each group was evaluated 3 days after surgery using the longa neural scoring method[66]. An open-field test was employed to detect the motor ability of mice. Mice were placed in the arena (40 × 40 × 40 cm) and allowed to move freely for 300 s. The motion trajectory was recorded by an infrared camera recording system (RWD) and motion trajectory, distances and mean speed in the zone were analyzed by the Smart analysis system (Panlab). A balance beam test was employed to investigate the balance ability of mice 3 days after MCAO. Mice were placed on the balance beam (40 × 3 cm) and the time spent on the balance beam was recorded (maximum recording time of 120 s).

Imaging data processing

To identify Inflare ROIs, all in vivo and acute slice imaging data were processed using AQuA[67] software in MATLAB (MathWorks). The Inflare persistence was quantified as an effective duration of signal above baseline. Regions with high fluorescence changes were automatically identified using the following parameters: intensity threshold scaling factor, 3.1; smoothing (sigma), 0.5; minimum size (pixels), 50; temporal cut threshold, 5; growing z threshold, 1; rising time uncertainty, 8; propagation smoothness, 2; z-score threshold, 2; maximum distance, 5; maximum correlation, 5; maximum time difference, 5; temporally extend events, Ture; ignore delay Tau, False, and the identified regions were further validated manually.

The migration index of microglia labeled in $Cx3cr1^{GFP/+}$ mice or stained by Iba1 was quantified as the relative fluorescence change in the injury center over the whole image. For cell morphology reconstruction and analysis, the number of neurons, microglia, astrocyte and apoptosis cells were evaluated using the spot function based on NeuN, Iba1, GFAP, cleaved caspase-3 IF staining or TUNEL-positive cells in Imaris 9.7 software; the length of processes, terminal points of branches, intersections of distance from the soma center and soma volume were measured based on Iba1 IF staining, using the filament and surface function. Analysis of microglia polarity was performed through the Imaris XT interface. Reconstruction of proliferating microglia or phagocytosis index/capacity was based on BrdU or TUNEL apoptotic cells engulfed by microglia using the surface function. Lysosome level was based on CD68 signal colocalized with Iba1 using the spot and surface function. For the cell-type-specific expression of Panx1, neurons and astrocytes were first reconstructed based on NeuN and GFAP staining, and the fluorescence staining images were enhanced by Aivia and then masked with Panx1 using Imaris. The fluorescence intensity of Panx1 was quantified using ImageJ.

Linear regression model

A toolbox based on relevance vector regression support vector machine was used to model the relationship between Inflares and injury. The injury intensity characterized by the damage size from Inflares after FLA. The original code used in the study is publicly available on GitHub at https://github.com/ZaixuCui/Pattern_Regression_Clean (ref. 68). Specifically, the support vector machine was implemented using a circular approach, where the z-score of datasets was randomly divided into five separate groups, four groups as a training set to predict the remaining group. The final accuracy was obtained by averaging the correlation weight over five iterations.

Statistical analysis

All summary data were presented as mean ± s.e.m. unless otherwise specified, with error bars representing s.e.m. No data were excluded

from the analysis. All data met the assumptions of the statistical tests used. Pearson's omnibus normality test was used to evaluate the normality and equality of variances between groups. For paired groups, the statistic difference was determined using a paired Student's t-test. For unpaired groups, an F-test was first performed to compare the variance, followed by a Student's t-test. A Mann–Whitney U-test was performed to compare differences between two independent groups when the dependent variable was either ordinal or continuous, but not normally distributed. A one-way analysis of variance was used to determine whether there were any statistically significant differences between the means of three independent (unrelated) groups. $P > 0.05$ was deemed not significant (NS). $*P < 0.05$; $**P < 0.01$; $***P < 0.001$.

Reporting summary

Further information on research design is available in the Nature Portfolio Reporting Summary linked to this article.

Data availability

The raw data in each figure have been provided as Source Data Files. The raw data related to RNA sequencing results have been deposited in the NCBI Sequence Read Archive database under accession codes SRR28644876 to SRR28644899. Other data reported in this paper will be shared by the corresponding author upon request. Source data are provided with this paper.

Code availability

The imaging data were processed by MATLAB 2018 (MathWorks) and Imaris 9.7 (Oxford University) and fluorescence intensity was quantified using ImageJ 1.53q (National Institutes of Health). The figures were organized using Adobe Illustrator 2023 (Adobe). The AQuA parameters used for identifying Inflare in this article, along with the analysis scripts based on AQuA results and the scripts for analyzing the sequencing results presented in this paper, can be accessed via GitHub at https://github.com/JingMiaoLab/NN82582C/tree/main.

References

62. Patriarchi, T. et al. Ultrafast neuronal imaging of dopamine dynamics with designed genetically encoded sensors. *Science* **360**, eaat4422 (2018).
63. Jing, M. et al. An optimized acetylcholine sensor for monitoring in vivo cholinergic activity. *Nat. Methods* **17**, 1139–1146 (2020).
64. Liu, F. et al. Changes in experimental stroke outcome across the life span. *J. Cereb. Blood Flow. Metab.* **29**, 792–802 (2009).
65. Hurn, P. D. & Macrae, I. M. Estrogen as a neuroprotectant in stroke. *J. Cereb. Blood Flow. Metab.* **20**, 631–652 (2000).
66. Longa, E. Z., Weinstein, P. R., Carlson, S. & Cummins, R. Reversible middle cerebral artery occlusion without craniectomy in rats. *Stroke* **20**, 84–91 (1989).
67. Wang, Y. et al. Accurate quantification of astrocyte and neurotransmitter fluorescence dynamics for single-cell and population-level physiology. *Nat. Neurosci.* **22**, 1936–1944 (2019).
68. Cui, Z. & Gong, G. The effect of machine learning regression algorithms and sample size on individualized behavioral prediction with functional connectivity features. *Neuroimage* **178**, 622–637 (2018).

Author contributions

Y.C. performed experiments related to ATP imaging and analysis of signal encoding. P.L. conducted experiments related to cell and molecular mechanism in vivo and MCAO-related experiments. J.L. carried out experiments related to signal decoding by microglia. Y.W. performed experiments for studying molecular mechanisms. C.W. designed and validated shRNA and sgRNA for genetic manipulations. R.W. performed the biochemical analysis of Panx1. Z.W. engineered the ATP1.0 sensor and made sensors expressing AAV constructs. M.J. conceived the project and performed brain slice experiments. All authors contributed to data analysis. Y.C. and M.J. wrote the manuscript with input from all the other authors.

Competing interests

The authors declare no competing interests.

Additional information

Extended data is available for this paper at https://doi.org/10.1038/s41593-024-01680-w.

Supplementary information The online version contains supplementary material available at https://doi.org/10.1038/s41593-024-01680-w.

Correspondence and requests for materials should be addressed to Miao Jing.

Peer review information *Nature Neuroscience* thanks Alexandre Charlet, Adam Cohen, Amanda Sierra, and the other, anonymous reviewer(s) for their contribution to the peer review of this work.

Reprints and permissions information is available at www.nature.com/reprints.

Population microglia analysis
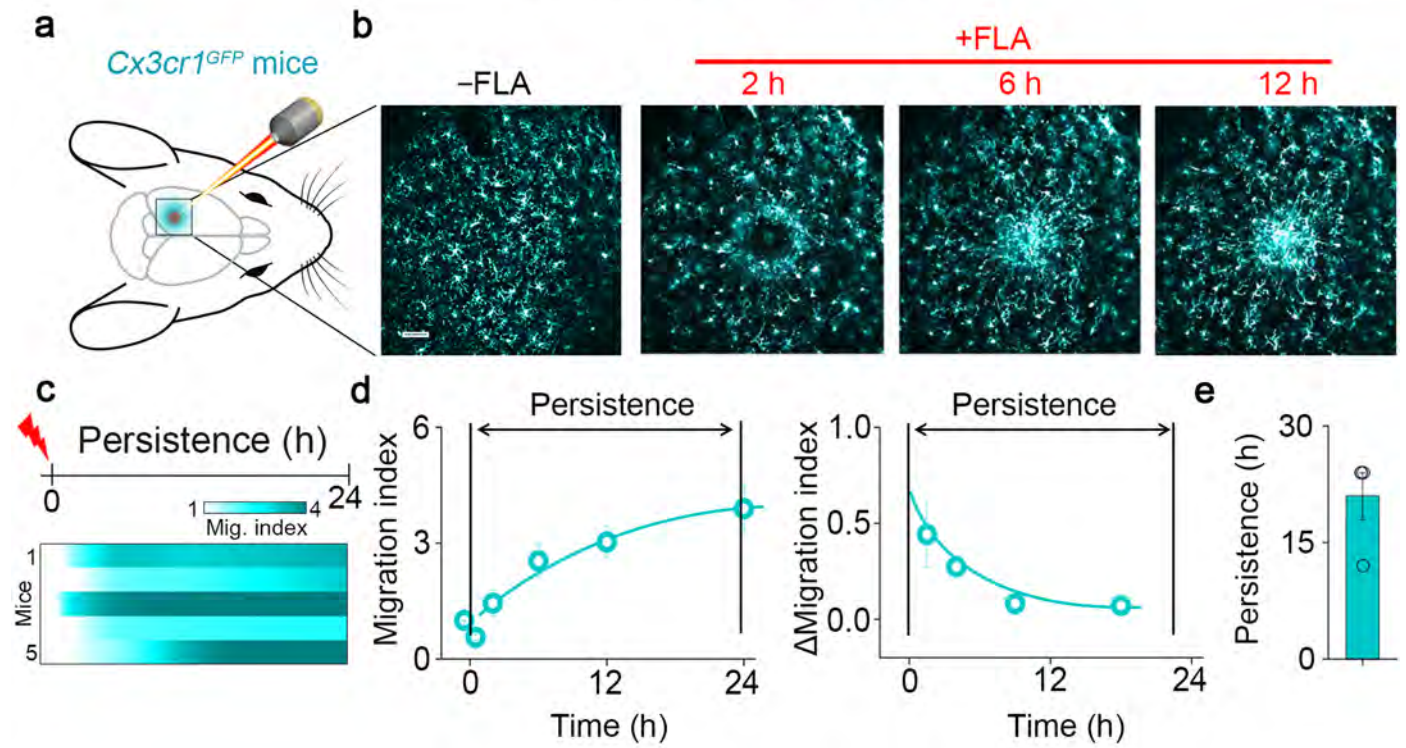
Single microglia analysis
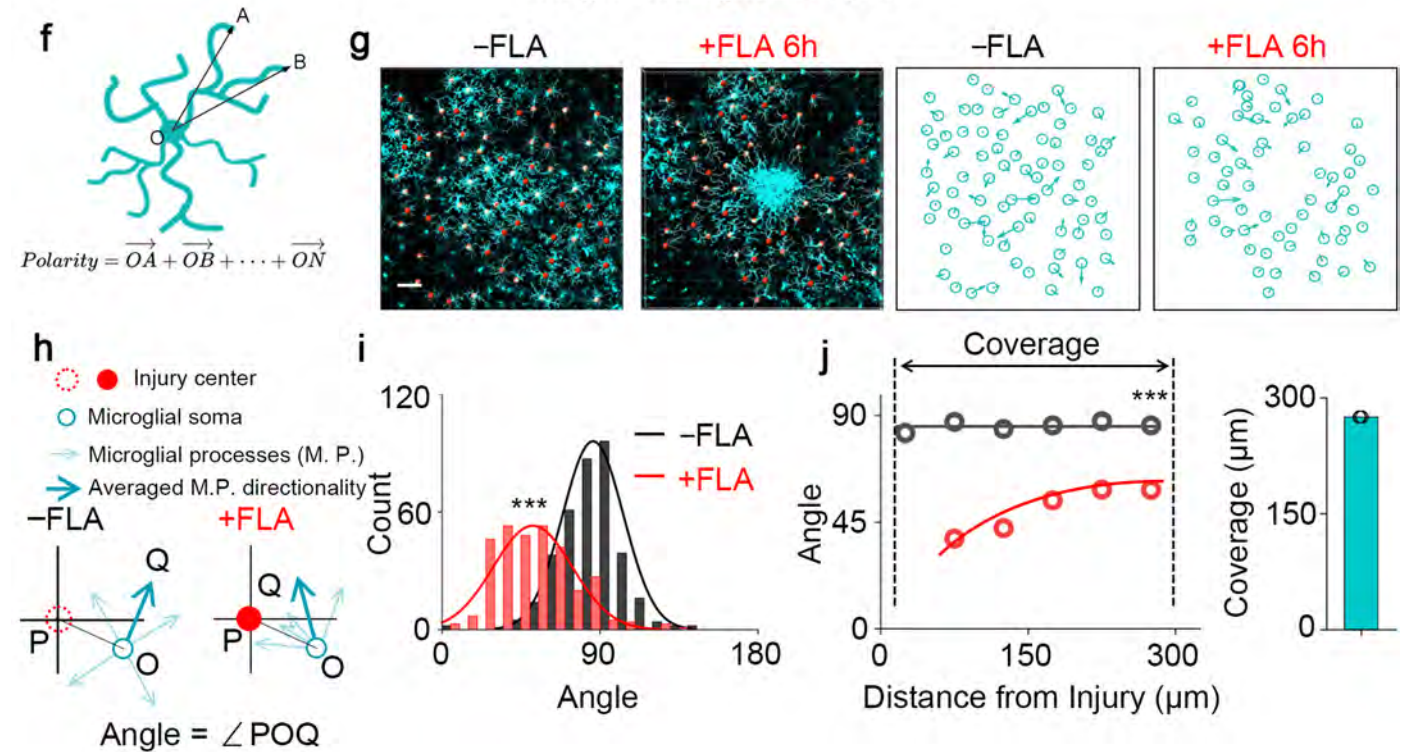
Extended Data Fig. 1 | See next page for caption.

Extended Data Fig. 1 | The spatiotemporal property of microglia motility after FLA injury. a. Illustration of experiments in which microglia motility was monitored in awake *Cx3cr1*$^{GFP/+}$ mice *in vivo*. Focal laser ablation (FLA) was used to introduce local injury, and two-photon imaging was conducted to track microglia. **b**. Representative images of microglia prior to FLA (−FLA) or after FLA at indicated time points. **c-e**. Time-dependent changes of microglia migration after FLA. The migration index is quantified as the relative fluorescence change in the injury center (180 μm in diameter) over the whole image. The data of each mouse are shown in (**c**), and averaged data as well as the changes of migration index over time (Δmigration index) are plotted in (**d**) (n = 5 mice). The persistence is the time with effective signal over baseline in (**e**) (n = 5 mice). **f**. Illustration of the measurement of microglia polarity. **g**. The changes of microglia polarity to FLA at the single cell level. **h**. Illustration of the microglia directionality towards the injury center. The angle between the microglia polarity and injury is quantified. **i**. The microglia directionality before (−FLA) and after FLA (n = 366 microglia from 5 mice for −FLA; n = 313 microglia from 5 mice for +FLA). **j**. The relationship between microglia directionality and the distance of microglia to injury. The area with signal above baseline (−FLA) is defined as coverage and quantified (n = 5 mice). Scale bars, 50 μm. Data are shown as the mean ± s.e.m. ***, $p < 0.001$; All statistical tests are two-sided and see Supplementary Table 1 for statistics.
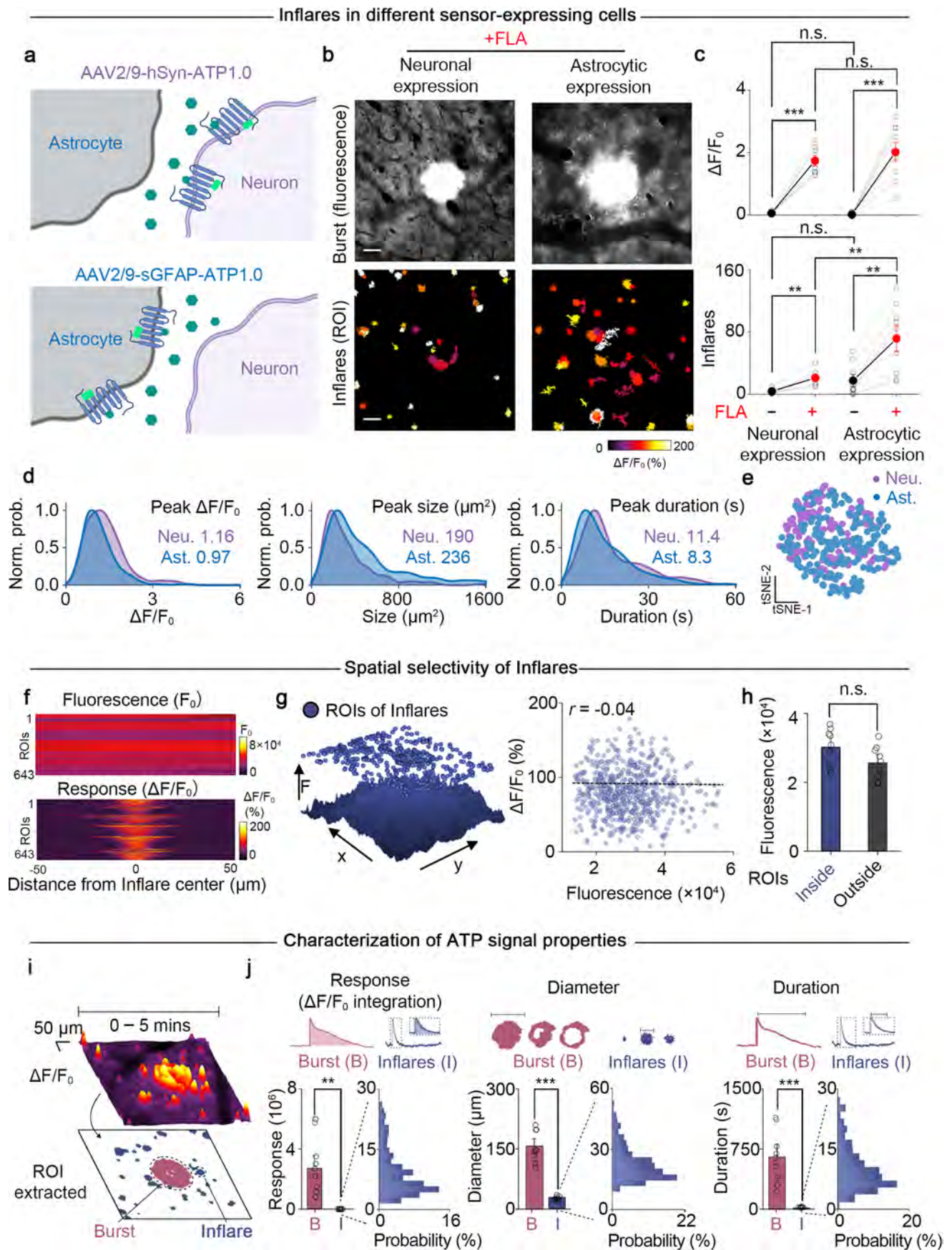
Extended Data Fig. 2 | See next page for caption.

Extended Data Fig. 2 | Characterization of injury-evoked ATP dynamics. a. Illustration of ATP1.0 sensors that are specifically expressed on the membrane of neurons (up) or astrocytes (bottom) in detecting extracellular ATP. **b.** The ATP burst (fluorescence image, up) and Inflares (ROI, bottom) in neuronal or astrocytic ATP1.0-expressing mice. **c.** The $\Delta F/F_0$ of ATP bursts (up) and the number of Inflares (bottom) before and after FLA, in neuronal or astrocytic ATP1.0-expressing mice ($n = 7$ and 9 mice for neuronal and astrocytic expression). **d. e**, The comparison of Inflares in neuronal or astrocytic ATP1.0-expressing mice, with properties include $\Delta F/F_0$, size and duration analyzed ($n = 7$ and 9 mice for neuronal and astrocytic expression). **f.** The spatial distribution of basal fluorescence (F_0) and fluorescence response ($\Delta F/F_0$) in Inflares. The Inflare ROIs are aligned with their center at position 0, and signals are plotted across 100 μm in space ($n = 643$ ROIs from $n = 9$ mice). **g.** The spatial distribution (left) and the correlation (right) of the $\Delta F/F_0$ with corresponding F_0 in Inflares ($n = 643$ Inflares from $n = 9$ mice; $r = -0.04$ by Pearson correlation analysis). **h.** The comparison of ATP1.0 fluorescence inside or outside of Inflare ROIs ($n = 9$ mice). **i.** The fluorescence response ($\Delta F/F_0$ in pseudocolor, up) and regions of interest (ROIs, bottom) extracted for analysis. **j.** Comparison of the fluorescence response ($\Delta F/F_0$ integration, left), diameter (middle) and duration (right) between ATP bursts and Inflares. Group data from each mouse are shown on the left, with the distribution of individual Inflares summarized on the right ($n = 643$ Inflares from $n = 9$ mice). Scale bars, 50 μm. Data are shown as the mean ± s.e.m. **, $p < 0.01$; ***, $p < 0.001$; n.s., not significant. All statistical tests are two-sided and see Supplementary Table 1 for statistics.
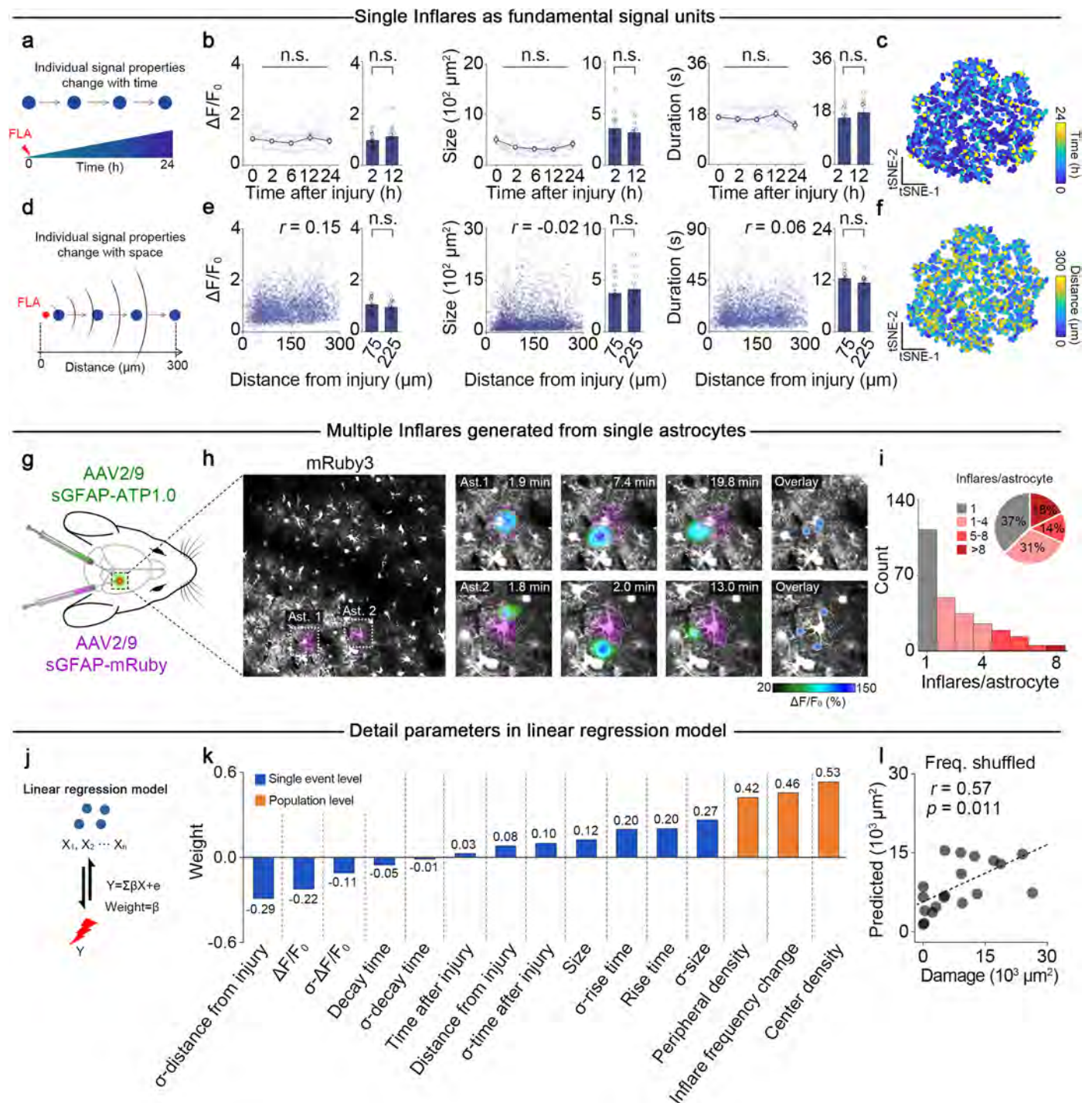
Extended Data Fig. 3 | Inflares are stereotyped and encode injury intensity by population frequency. a, b. The comparison of Inflares across time, with the fluorescence change ($\Delta F/F_0$, left), size (middle) and duration (right) analyzed ($n = 13$ mice). **c.** The dimensional reduction analysis of Inflares recorded across time ($n = 3980$ Inflares from 13 mice). **d-f.** Similar as **(a-c)**, except Inflares at different locations away from injury are analyzed ($n = 3980$ Inflares from 13 mice). **g, h.** Two-photon image of astrocytes co-expressing ATP1.0 and mRuby3. Two astrocytes were selected with their territory marked in magenta. Right, the generation of Inflares at selected time points in individual astrocytes.

The positions of Inflare generation are extracted and overlayed. **i.** The Inflare number from single astrocytes within 2 hours after FLA. **j.** Illustration of the linear regression model to predict injury from Inflares. **k.** Parameters of Inflare properties and their weights in the successful-trained linear regression model. **l.** The relationship between measured damage and Inflare-predicted damage using shuffled frequency data in the linear regression model ($n = 19$ mice). Data are shown as the mean ± s.e.m. n.s., not significant. All statistical tests are two-sided and see Supplementary Table 1 for statistics.
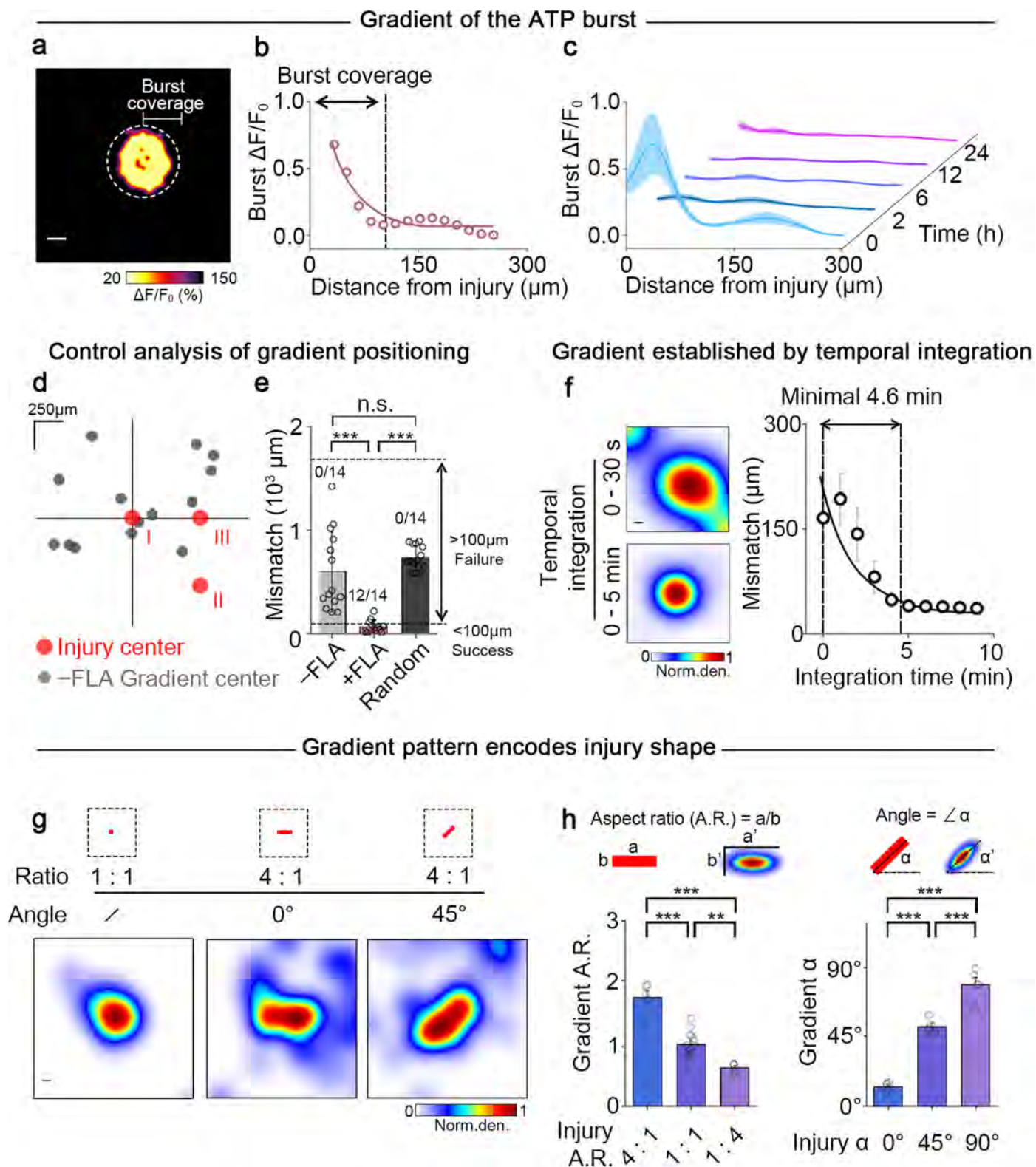
Extended Data Fig. 4 | Gradient distribution of Inflares encode injury position and shape. a-b. The gradient of ATP burst (in $\Delta F/F_0$) with distance over injury ($n = 13$ mice). **c.** Changes of ATP burst ($\Delta F/F_0$) at indicated time points after FLA. **d.** The alignment of FLA centers (red) with Inflare gradient centers recorded prior to the FLA (−FLA, gray) ($n = 14$ mice). **e.** The mismatch distance between Inflare gradient centers and FLA centers. The Inflares recorded prior to FLA (−FLA), after FLA (+FLA) or random generated signals with same frequency (Random) are analyzed. Mismatches less than 100 µm are defined as success,

and the success rate of each group is labeled ($n = 14$ mice for each group). **f.** Left, comparison of gradients that integrated Inflares over indicated time periods. Right, the relationship between gradient robustness (mismatch of gradient center with FLA center) and integration time. **g-h.** Inflare gradients with the alteration of injury shapes ($n = 5/14/5$ mice for gradient A.R, $n = 5/5/5$ mice for gradient α, respectively). Scale bars, 50 µm. Data are shown as the mean ± s.e.m. *, $p < 0.05$; **, $p < 0.01$; ***, $p < 0.001$; n.s., not significant. All statistical tests are two-sided and see Supplementary Table 1 for statistics.
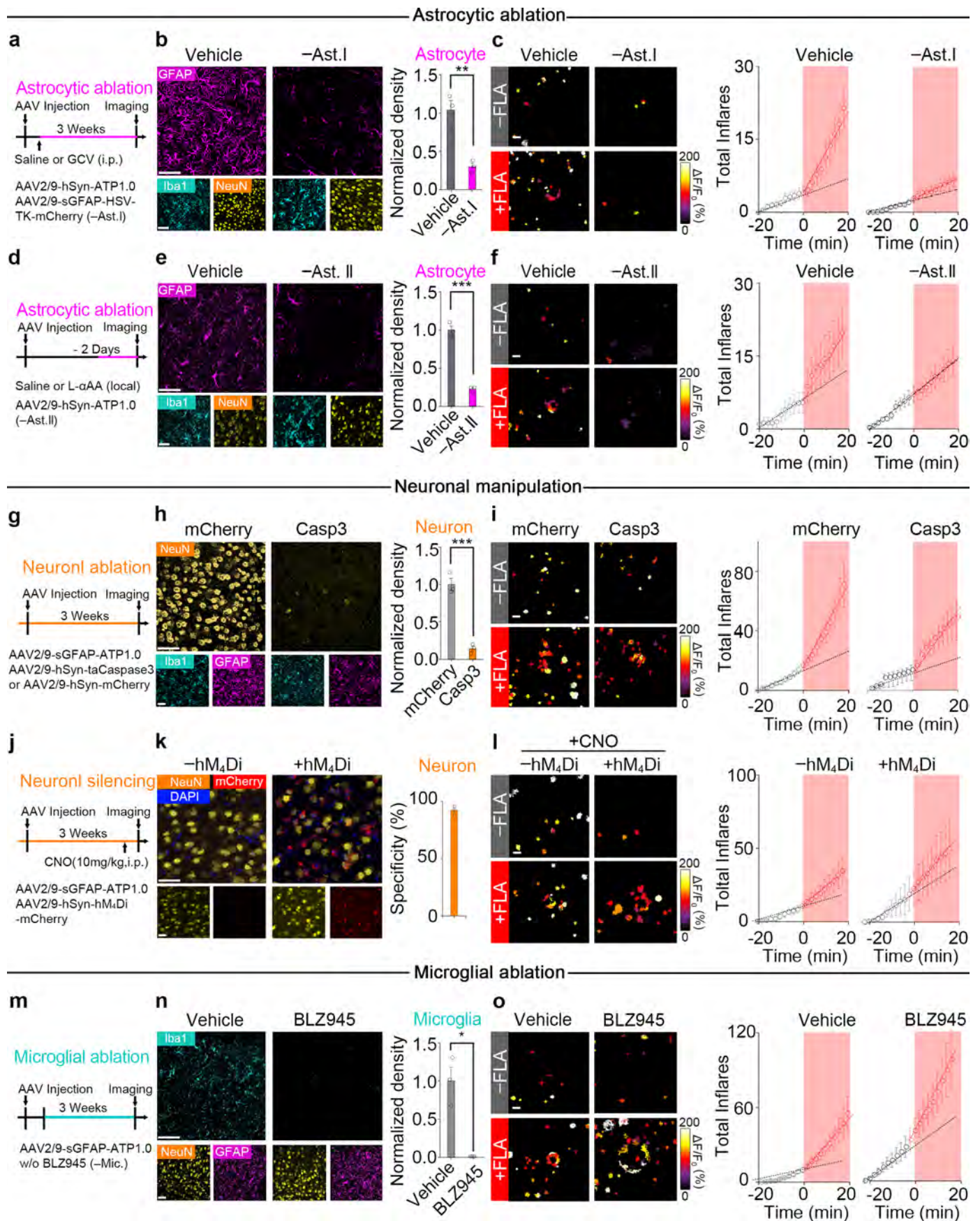
Extended Data Fig. 5 | See next page for caption.

Extended Data Fig. 5 | The cellular source of Inflares. a. Illustration of experiments in which astrocytes were locally ablated by HSV-TK expression and GCV application (-Ast.I), and FLA-evoked Inflares were recorded by neuronal-expressed ATP1.0 sensors. The HSV-TK expressing mice with saline injection were used as controls (Vehicle). **b**. Different cell types in Vehicle or -Ast.I mice ($n = 3$ mice). **c**. Inflares in Vehicle or astrocyte-ablated mice (-Ast.I) ($n = 6$ mice). **d-f**. Similar as (a-c), except astrocytes were ablated by injection of gliotoxin L-αAA (-Ast.II). Mice with saline injection were used as controls (Vehicle) ($n = 3$ mice for staining; $n = 6$ mice in Vehicle and $n = 7$ mice in -Ast.II for recording). **g**–**i**. The immunofluorescence images and FLA-evoked Inflares in mice with local ablation of neurons by taCaspase3 (Casp3). The specificity is quantified as the colocalization of mCherry with NeuN. Mice with mCherry expression were used as controls ($n = 3$ mice for staining; $n = 5$ mice in mCherry and $n = 4$ mice in Casp3 for recording). **j**–**l**. The immunofluorescence images and FLA-evoked Inflares in mice with neuron inhibition. Mice injected with CNO without neuronal hM_4Di expression ($-hM_4Di$) were used as controls ($n = 3$ mice for staining; $n = 4$ mice for recording). **m-o**. The immunofluorescence images and FLA-evoked Inflares in mice with microglia depletion by BLZ945. Mice fed with normal food (Vehicle) were used as controls ($n = 3$ mice for staining; $n = 8$ mice in Vehicle and $n = 9$ mice in BLZ945 for recording). Scale bars, 50 μm. Data are shown as the mean ± s.e.m. *, $p < 0.05$; **, $p < 0.01$; ***, $p < 0.001$. All statistical tests are two-sided and see Supplementary Table 1 for statistics.
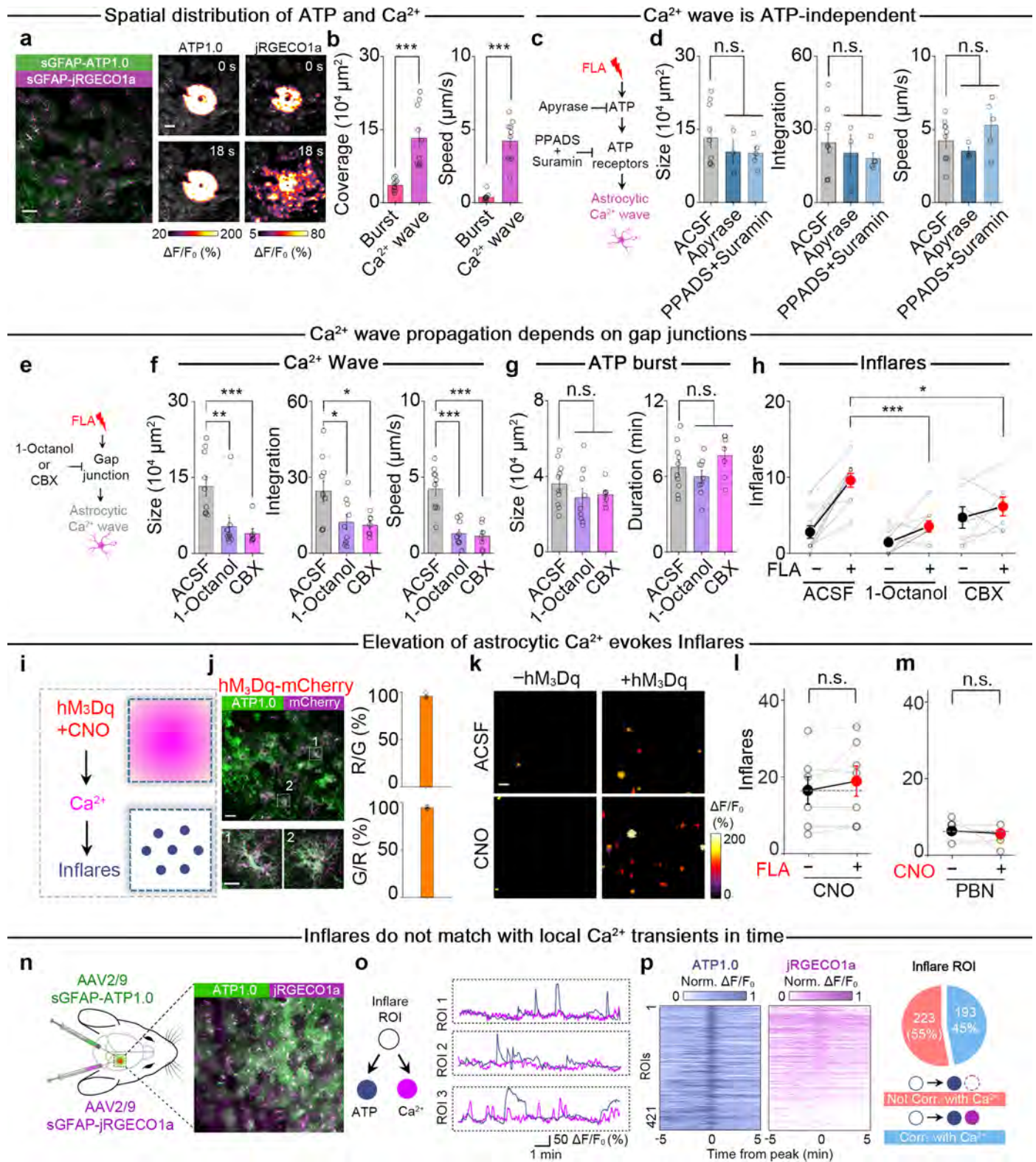
Extended Data Fig. 6 | See next page for caption.

Article

Extended Data Fig. 6 | Inflares depend on astrocytic Ca²⁺ signaling. a. The expression (left) and fluorescence response (right) of ATP1.0 sensor (green) and jRGECO1a (red) co-expressed in astrocytes *in vivo*. **b**. The maximum spatial coverage (left) and average propagation speed (right) of ATP burst and astrocytic Ca²⁺ wave after injury (n = 10 slices from 4 mice). **c, d**. The ATP-dependency of FLA-evoked astrocytic Ca²⁺ wave, with its maximum propagation size (left), integration of fluorescence changes (middle) and propagation speed (right) analyzed (n = 10/3/5 slices from 4/2/3 mice for ACSF, apyrase and PPADS + Suramin). **e-g**. The gap-junction dependency of FLA-evoked astrocytic Ca²⁺ wave (f) and ATP bursts (g) (n = 10/9/7 slices from 4/4/3 mice for ACSF, 1-Octanol and CBX). **h**. FLA-evoked Inflares with gap-junction blockers (n = 10/9/7 slices from 4/4/3 mice for ACSF, 1-Octanol and CBX). **i, j**. Co-expression of hM₃Dq

(magenta) and ATP1.0 (green) in astrocytes for chemogenetic activation by CNO (n = 4 mice). **k, l**. Inflares in hM₃Dq-expressing or control (−hM₃Dq) slices with CNO application (n = 7 slices from 3 mice). **m**. CNO-evoked Inflares in hM₃Dq-expressing slices bathed with PBN (n = 4 slices from 2 mice). **n, o**. Analysis of the colocalization of ATP and Ca²⁺ signals in mice co-expressing ATP1.0 and jRGECO1a in astrocytes. **p**. Left, alignment of Inflares peak and its corresponding Ca²⁺ signals. Right, the pie graph showing the distribution of Inflares that are either paired or non-paired with simultaneous Ca²⁺ elevation (n = 421 Inflares). Scale bars, 50 μm, except 5 μm in (**j**) (bottom). Data are shown as the mean ± s.e.m. *, $p < 0.05$; **, $p < 0.01$; ***, $p < 0.001$; n.s., not significant. All statistical tests are two-sided and see Supplementary Table 1 for statistics.
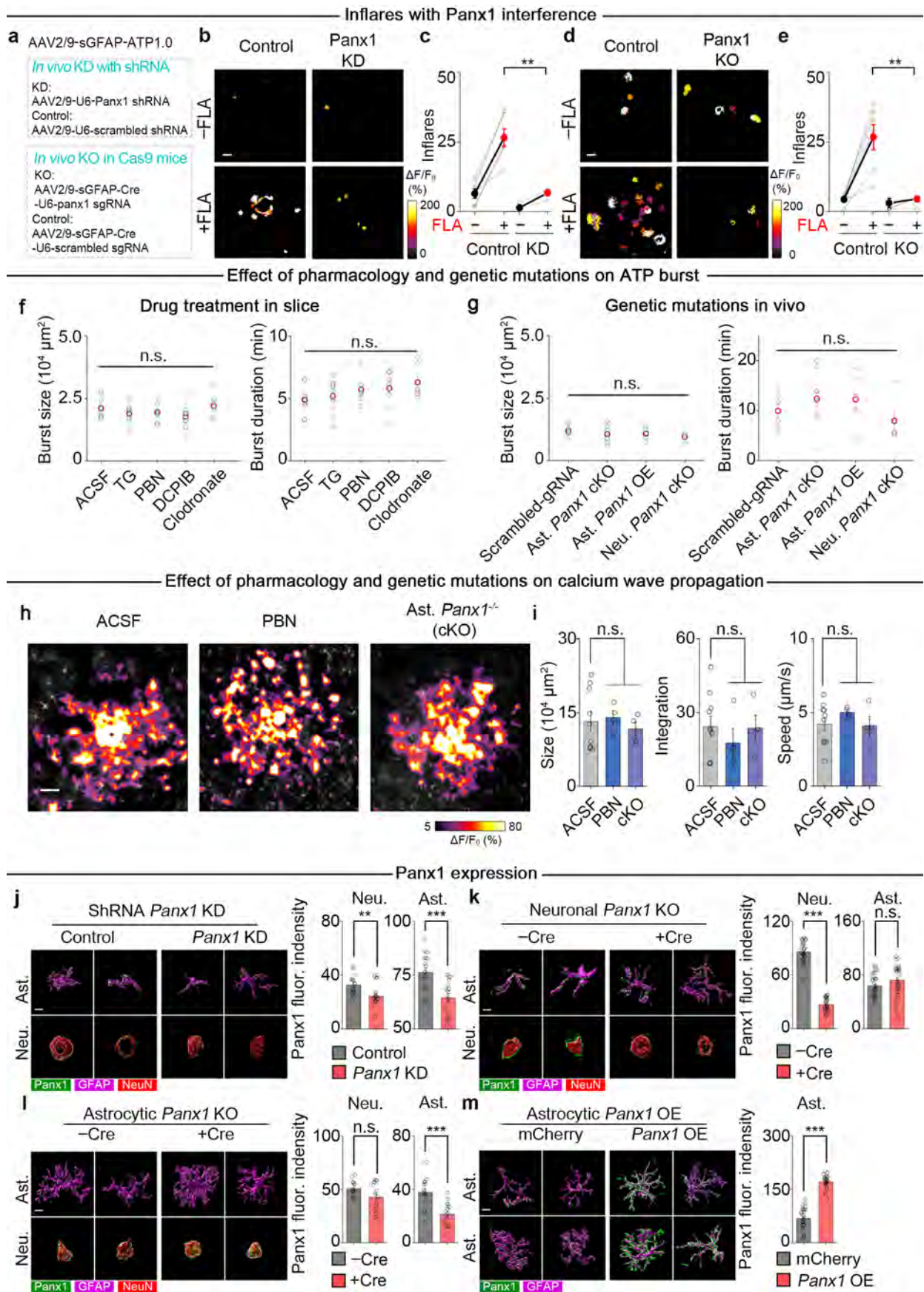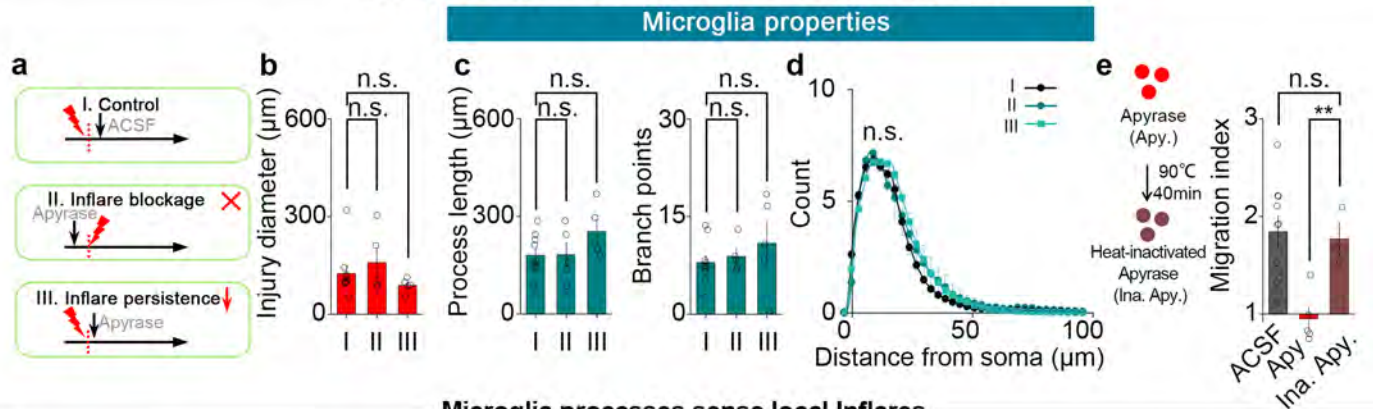
Extended Data Fig. 7 | See next page for caption.

**Extended Data Fig. 7 | Inflares depend on astrocytic Panx1 hemichannels.**
a. Illustration of *Panx1* knockdown (KD, up), or knockout (KO, bottom) in
Cas9-expressing mice. Scrambled shRNA or sgRNA were used as control. **b,**
c. FLA-evoked Inflares in scrambled-shRNA-expressing (control) or *Panx1*
knockdown (*Panx1* KD) mice (*n* = 5 and 3 mice for the control and *Panx1* KD).
d, e. Similar as **(b-c)**, except Inflares were recorded in *Panx1*-sgRNA expressing
Cas9 mice (*Panx1* KO) or scrambled-sgRNA expressing Cas9 mice (control) (*n* = 6
and 4 mice for control and *Panx1* KO). **f**. The size (left) and persistence (right) of
FLA-evoked ATP burst in slices treated with ACSF, thapsigargin (TG), PBN, DCPIB
or Clodronate (*n* = 10/11/7/9/7 slices from each group from *n* = 3 mice). **g**. Similar
as **(f)**, except the ATP burst in different genetic manipulations are analyzed (*n* = 6
mice for scrambled-sgRNA mice; *n* = 9 mice for astrocytic *Panx1* knockout mice;
n = 5 mice for astrocytic Panx1 OE mice; *n* = 5 mice for neuronal *Panx1* knockout
mice). **h, i**. The astrocytic Ca²⁺ wave in ACSF-treated, PBN-treated slices or slices
from astrocytic *Panx1* knockout mice (cKO) (*n* = 10/4/4 slices from 4/2/2 mice for
ACSF, PBN and cKO). **j-m**. The Panx1 protein expression in astrocytes (Ast., up)
and neurons (Neu., bottom) in each experimental condition (*n* = 18/30/16/29 cells
from each group from *n* = 2 mice). Scale bars, 50 μm for **(b) (d)** and **(h)**, and 10 μm
for **(j-m)**. Data are shown as the mean ± s.e.m. *, *p* < 0.05; **, *p* < 0.01; ***, *p* < 0.001;
n.s., not significant. All statistical tests are two-sided and see Supplementary
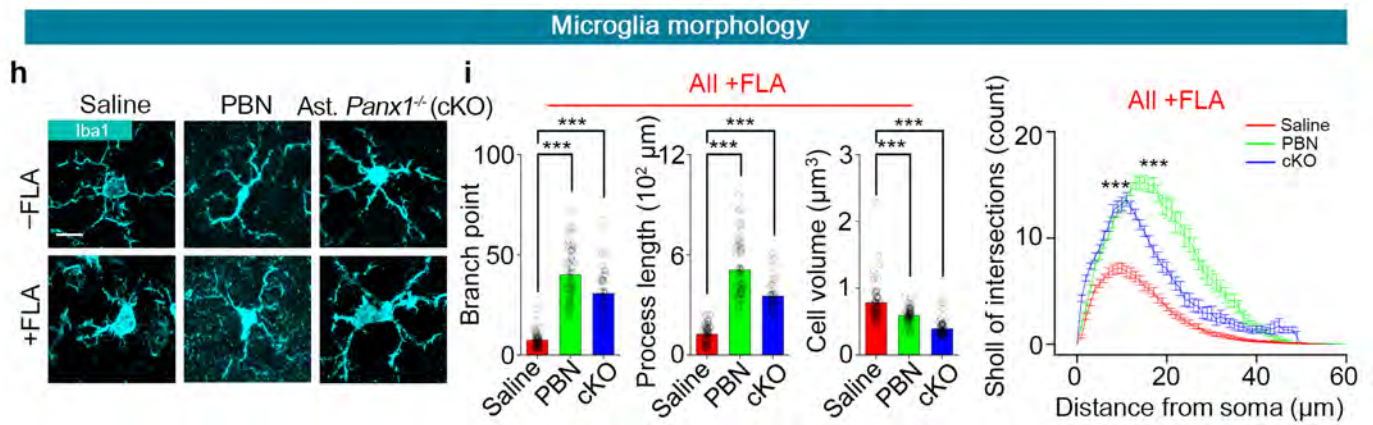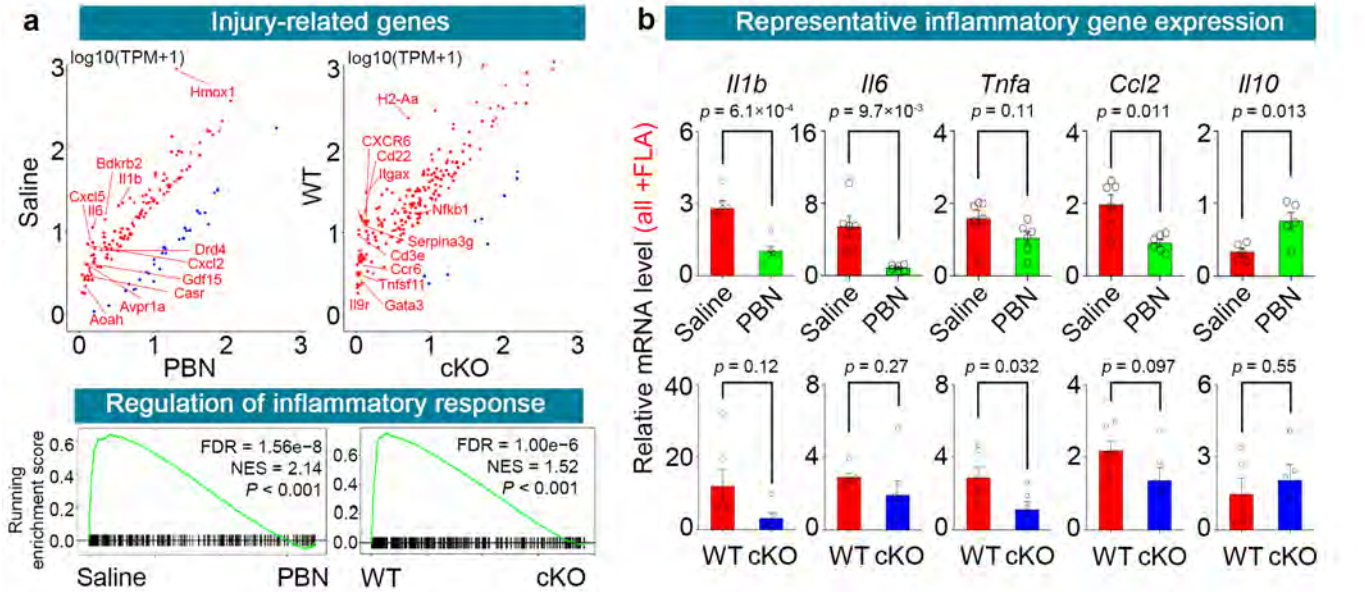Table 1 for statistics.
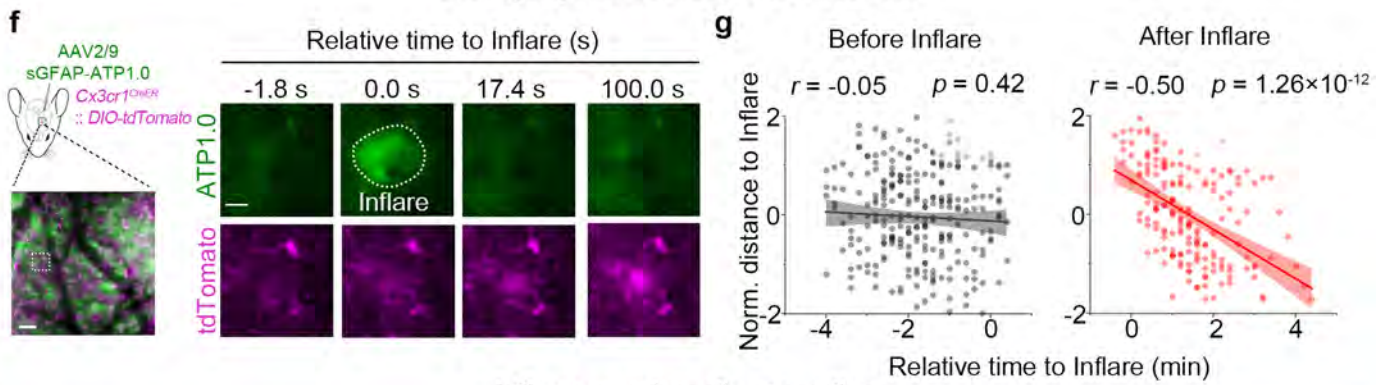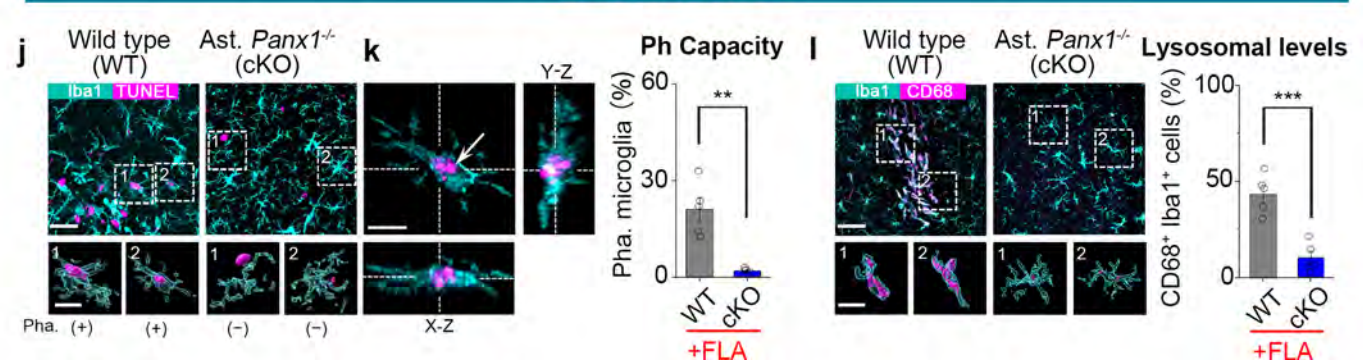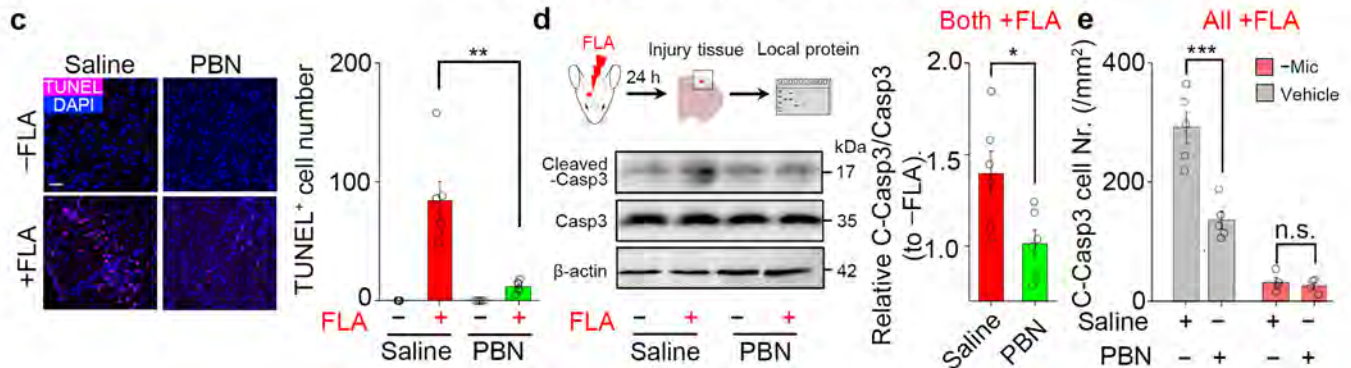
Extended Data Fig. 8 | See next page for caption.

Extended Data Fig. 8 | Inflares drive changes in microglia states. a. Schematic of experimental design in which total Inflares (II) or persistent Inflares (III) were abolished *in vivo*. ACSF injection was used as control (I). **b**. The injury diameter in each group (n = 10/5/5 mice in I, II and III). **c, d**. The microglia morphology in different groups in *Cx3cr1*^GFP mice (n = 10/5/5 mice in I, II and III group, respectively). **e**. The FLA-evoked microglia migration in ACSF, apyrase (Apy) or inactivated apyrase (Ina. Apy) injected mice (n = 10/5/3 mice in ACSF, apyrase and inactivated apyrase group). **f.** Local extension of microglia processes (tdtomato, magenta) towards an Inflare (ATP1.0, green). **g.** The distance of each microglia process towards the Inflare center before and after the occurrence of an Inflare (n = 21/20 microglia). **h, i**. Microglia morphology (Iba1, cyan) in saline or PBN-injected mice, or in astrocytic *Panx1* knockout mice (Ast. *Panx1*^{−/−}, cKO) (cell volume: n = 58/6 cells/mice in saline, PBN and cKO; others: n = 63/6, 55/6

and 40/5 cells/mice in each group). **j.** The microglia (Iba1, cyan) phagocytosing apoptotic cells (TUNEL, magenta) in wild type (WT) or Ast. *Panx1*^{−/−} (cKO) mice at 8 h after FLA. The Selected microglia are zoomed in with their phagocytosis states annotated as positive (+) or negative (−). **k.** Left, the 3D image showing the pouch of microglia process surrounding the apoptotic cell. Right, quantification of phagocytosis capacity at 8 h after FLA in WT and cKO mice. The phagocytosis capacity is defined as the percentage of microglia which are phagocytosing (n = 5 mice). **l.** Colocalization of lysosome marker (CD68, magenta) with microglia in WT or cKO mice at 8 h after FLA (n = 5 mice). Scale bars, 50 μm in (**h, j, up**), and 10 μm in (**f, i**) and reconstructed cells in (**h, j, bottom**). Data are shown as the mean ± s.e.m. *p < 0.05; **p < 0.01; ***p < 0.001; n.s., not significant. All statistical tests are two-sided and see Supplementary Table 1 for statistics.

Extended Data Fig. 9 | Inflares affect injury-induced transcriptional changes and cell apoptosis. a. Expression profiling of injury-related genes (up) and enrichment analysis of inflammatory pathway gene (bottom) between saline and PBN-injected mice (left), or between wild type (WT) and astrocytic *Panx1* knockout (cKO) mice 24 h after FLA (*n* = 3 mice). **b**. The expression level of inflammatory-related genes 24 h after FLA by real-time quantitative PCR, between saline- and PBN-injected mice (up), or between WT and cKO mice (bottom) (*n* = 6 mice). **c**. The apoptotic cells (TUNEL+, red) in saline or PBN-treated mice at 8 h after FLA (*n* = 6 mice). **d**. The protein level of cleaved caspase-3 (C-Casp3) and caspase-3 (Casp3), in saline or PBN-treated mice at 8 h after FLA (*n* = 6 mice). Quantitative comparison of C-Casp3 and Casp3 sample from same blot. The β-actin was used as the internal control from same experiments. **e**. Number of apoptotic cells (C-casp3+) at 8 hours after FLA, in control (Vehicle) or microglia-depleted (−Mic.) mice treated with saline or PBN (*n* = 5/4 mice in Vehicle and −Mic. group). Scale bars, 50 μm in **(c)**. Data are shown as the mean ± s.e.m. *$p < 0.05$; **$p < 0.01$; ***$p < 0.001$; n.s., not significant. All statistical tests are two-sided and see Supplementary Table 1 for statistics.
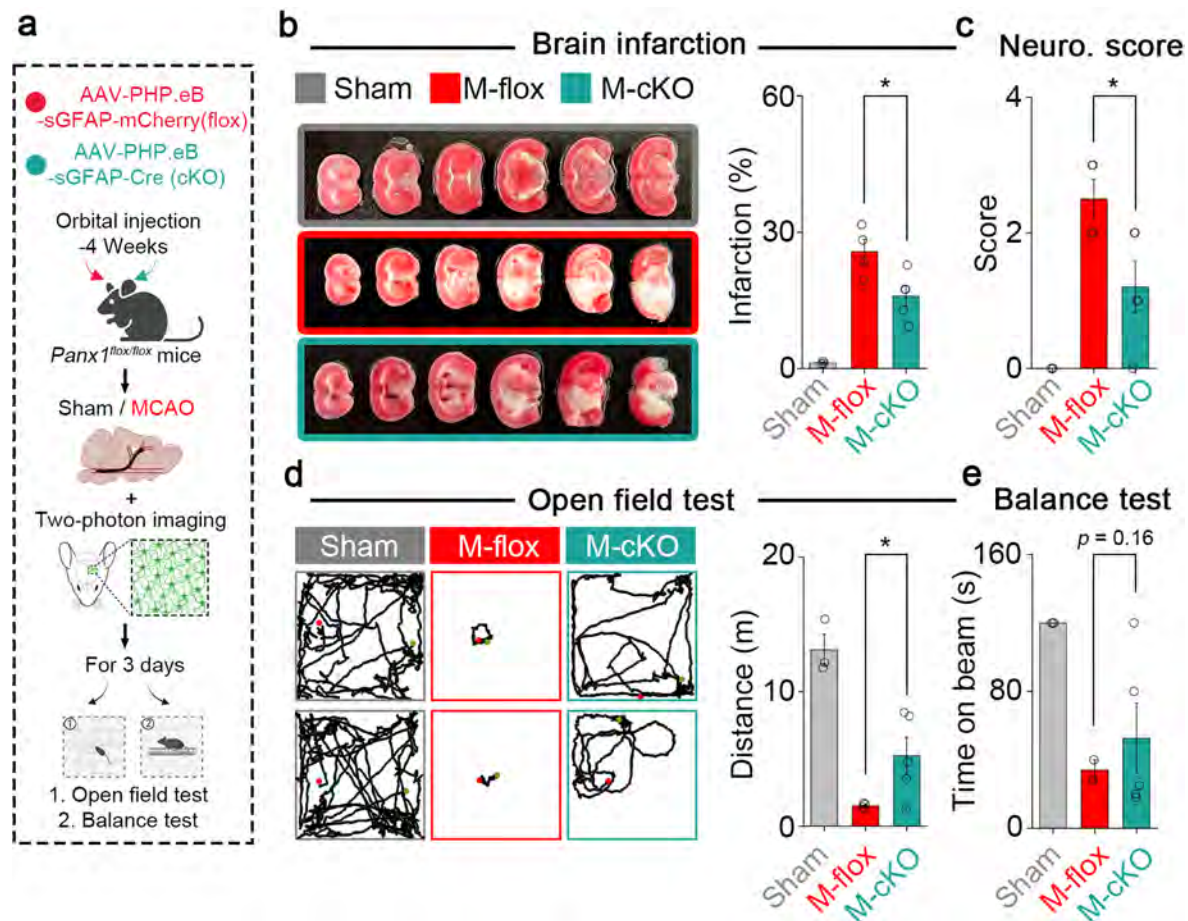
Extended Data Fig. 10 | Knocking out astrocytic Panx1 shows protective effect for ischemic stroke in mice. a. The consequence of Inflare blockage by astrocytic *Panx1* knockout on MCAO outcome. The AAV-PHP. eB with astrocytic expressing of mCherry or cre was orbitally injected into the *Panx1*^flox/flox mice for whole brain astrocytic *Panx1* knockout. **b**. The brain infarction in Sham, flox mice with MCAO (M-flox) or astrocytic *Panx1* knockout mice with MCAO (M-cKO) at 3 days after surgery, $p = 0.027$ between M-flox and M-cKO. **c**. The neurological deficient scores in different groups at 3 days after surgery ($n = 3$ mice for Sham; $n = 4$ mice for M-flox; $n = 5$ mice for M-cKO). **d**. The trajectory of mice (left) and total movement distances (right) in the open field test over 5 minutes ($n = 3$ mice for Sham; $n = 4$ mice for M-flox; $n = 5$ mice for M-cKO). **e**. The total time that mice maintained on the balance beam ($n = 3$ mice for Sham; $n = 4$ mice for M-flox; $n = 5$ mice for M-cKO). Scale bars, 50 μm. Data are shown as the mean ± s.e.m. *, $p < 0.05$; All statistical tests are two-sided and see Supplementary Table 1 for statistics.

Corresponding author(s): Miao Jing

Last updated by author(s): May 12, 2024

Reporting Summary

Nature Portfolio wishes to improve the reproducibility of the work that we publish. This form provides structure for consistency and transparency in reporting. For further information on Nature Portfolio policies, see our Editorial Policies and the Editorial Policy Checklist.

Statistics

For all statistical analyses, confirm that the following items are present in the figure legend, table legend, main text, or Methods section.

n/a	Confirmed	
☐	☒	The exact sample size (*n*) for each experimental group/condition, given as a discrete number and unit of measurement
☐	☒	A statement on whether measurements were taken from distinct samples or whether the same sample was measured repeatedly
☐	☒	The statistical test(s) used AND whether they are one- or two-sided *Only common tests should be described solely by name; describe more complex techniques in the Methods section.*
☐	☒	A description of all covariates tested
☐	☒	A description of any assumptions or corrections, such as tests of normality and adjustment for multiple comparisons
☐	☒	A full description of the statistical parameters including central tendency (e.g. means) or other basic estimates (e.g. regression coefficient) AND variation (e.g. standard deviation) or associated estimates of uncertainty (e.g. confidence intervals)
☐	☒	For null hypothesis testing, the test statistic (e.g. *F*, *t*, *r*) with confidence intervals, effect sizes, degrees of freedom and *P* value noted *Give P values as exact values whenever suitable.*
☒	☐	For Bayesian analysis, information on the choice of priors and Markov chain Monte Carlo settings
☒	☐	For hierarchical and complex designs, identification of the appropriate level for tests and full reporting of outcomes
☐	☒	Estimates of effect sizes (e.g. Cohen's *d*, Pearson's *r*), indicating how they were calculated

Our web collection on statistics for biologists contains articles on many of the points above.

Software and code

Policy information about availability of computer code

Data collection	No special code was used for data collection.
Data analysis	Software: The imaging data was processed by Matlab 2018 (Mathwork) and Imaris 9.7 (Oxford University), and fluorescence intensity was quantified using ImageJ 1.53q (National Institute of Health). The figures are organized using Adobe Illustrator 2023 (Adobe). Codes: The AQuA parameters used for identifying Inflare in this article, along with the analysis scripts based on AQuA results, and the scripts for analyzing the sequencing results presented in this paper, can be accessed via the GitHub link at [https://github.com/JingMiaoLab/NN82582C/tree/main].

For manuscripts utilizing custom algorithms or software that are central to the research but not yet described in published literature, software must be made available to editors and reviewers. We strongly encourage code deposition in a community repository (e.g. GitHub). See the Nature Portfolio guidelines for submitting code & software for further information.

Data

Policy information about availability of data

All manuscripts must include a data availability statement. This statement should provide the following information, where applicable:
- Accession codes, unique identifiers, or web links for publicly available datasets
- A description of any restrictions on data availability
- For clinical datasets or third party data, please ensure that the statement adheres to our policy

> The raw data in each figure have been provided as Source Data Files. The raw data related to RNA sequencing results have been deposited in the NCBI Sequence Read Archive (SRA) database with accession code SRR28644876 to SRR28644899 (link: https://www.ncbi.nlm.nih.gov/sra/SRR28644876 to https://www.ncbi.nlm.nih.gov/sra/SRR28644899). Other data reported in this paper will be shared by the lead contact upon request.

Research involving human participants, their data, or biological material

Policy information about studies with human participants or human data. See also policy information about sex, gender (identity/presentation), and sexual orientation and race, ethnicity and racism.

Reporting on sex and gender	No human participants or human data are involved in the study.
Reporting on race, ethnicity, or other socially relevant groupings	No human participants or human data are involved in the study.
Population characteristics	No human participants or human data are involved in the study.
Recruitment	No human participants or human data are involved in the study.
Ethics oversight	No human participants or human data are involved in the study.

Note that full information on the approval of the study protocol must also be provided in the manuscript.

Field-specific reporting

Please select the one below that is the best fit for your research. If you are not sure, read the appropriate sections before making your selection.

☒ Life sciences ☐ Behavioural & social sciences ☐ Ecological, evolutionary & environmental sciences

For a reference copy of the document with all sections, see nature.com/documents/nr-reporting-summary-flat.pdf

Life sciences study design

All studies must disclose on these points even when the disclosure is negative.

Sample size	No statistical methods are used to pre-determine sample size. Sample sizes are indicated for each experiment and are chosen based on similar previous studies, for example PMID: 29853555 and PMID: 32989318.
Data exclusions	No data is excluded from the analysis.
Replication	Each data in this manuscript is reliably reproducible. The replication number of each data is indicated in the legend of corresponding figures.
Randomization	Animals or cells are randomly assigned into experimental or control groups.
Blinding	Investigators are blinded to the group allocation during experiments.

Reporting for specific materials, systems and methods

We require information from authors about some types of materials, experimental systems and methods used in many studies. Here, indicate whether each material, system or method listed is relevant to your study. If you are not sure if a list item applies to your research, read the appropriate section before selecting a response.

Materials & experimental systems

n/a	Involved in the study
☐	☒ Antibodies
☒	☐ Eukaryotic cell lines
☒	☐ Palaeontology and archaeology
☐	☒ Animals and other organisms
☒	☐ Clinical data
☒	☐ Dual use research of concern
☒	☐ Plants

Methods

n/a	Involved in the study
☒	☐ ChIP-seq
☒	☐ Flow cytometry
☒	☐ MRI-based neuroimaging

Antibodies

Antibodies used

Primary antibody including (1) rabbit anti-Iba1 (Abcam, #ab178846, 1:1000), (2) chicken anti-GFAP (Abcam, #ab4674, 1:1000), (3) rabbit anti-GFAP (Abcam, #ab7260, 1:1000), (4) rabbit anti-NeuN (Abcam, #ab177487, 1:1000), (5) mouse anti-NeuN (Abcam, #ab104224, 1:1000), (6) rabbit anti-GFP (Abcam, #ab290, 1:1000), (7) rat anti-BrdU (Abcam, #ab6326, 1:500), (8) rat anti-CD68 (Abcam, #ab53444, 1:500), (9) rabbit anti-pannxin1 (Thermo Fisher Scientific, #488100, 1:200), (10) rabbit anti-cleaved caspase-3 (Asp175) (CST, #9661, 1:1000), (11) rabbit anti-caspase-3 (CST, #9662, 1:1000), (12) mouse anti-β-actin (Abcam, #ab8226, 1:1000) were used.
Secondary antibody including (1) Alexa Fluor 488 goat anti-rabbit (Abcam, #ab150077, 1:1000), (2) Alexa Fluor 555 goat anti-rabbit (Abcam, #ab150078, 1:1000), (3) Alexa Fluor 488 goat anti-mouse IgG H&L (Abcam, #ab150113, 1:1000), (4) Alexa Fluor 555 goat anti-mouse (Abcam, #ab150114, 1:1000), (5) Alexa Fluor 647 goat anti-chicken (Abcam, #ab150171, 1:1000), (6) Alexa Fluor 647 goat anti-rat IgG H&L (Abcam, #ab150167), (7) Horseradish peroxidase (HRP)-conjugated goat anti-rabbit IgG (H+L) (Multi science, #GAR0072, 1:5000), (8) HRP-conjugated rabbit anti-mouse IgG (H+L) (Abcam, #ab6728, 1:1000) are used.

Validation

The rabbit anti-Iba1 (Abcam, #ab178846) used in immunofluorescence has been verified in Gangoso E, et al. Cell, 2021 and Masuda T, et al.. Nature, 2019.
The chicken anti-GFAP (Abcam, #ab4674) used in immunofluorescence has been verified in Müller FE, et al. Glia, 2021 and Gerbino V, et al. Neuron, 2020.
The rabbit anti-GFAP (Abcam, #ab7260) used in immunofluorescence has been verified in Singh G, et al. J Neuroinflammation, 2021 and Brodovskaya A, et al. Brain, 2021.
The rabbit anti-NeuN (Abcam, #ab177487) used in immunofluorescence has been verified in Yuan W, et al. Proc Natl Acad Sci U S A, 2021 and Fairley LH, et al. J Neuroinflammation, 2021.
The mouse anti-NeuN (Abcam, #ab104224) used in immunofluorescence has been verified in Courtland JL, et al. elife, 2021 and Bi WK, et al. Acta Pharmacol Sin, 2020.
The rabbit anti-GFP (Abcam, #ab290) used in immunofluorescence has been verified in Casarotto PC, et al, Cell. 2021 and Ashley GE, et al. Genetics, 2021.
The rat anti-BrdU (Abcam, #ab6326) used in immunofluorescene has been verified in Huerga-Gómez A, et al. Glia. 2021 and Qu M, et al. Stroke Vasc Neurol, 2021.
The rat anti-CD68 (Abcam, #ab53444) used in immunofluorescene has been verified in Brooks LJ, et al. Nat Commun. 2021 and Pinto B, et al. Neuron, 2020.
The rabbit anti-pannxin1 (Thermo Fisher Scientific, #488100) used in immunofluorescene has been verified in Lana J M, et al. BMC neuroscience, 2011 and Ryan C F Siu, et al. Communications biology, 2021.
The rabbit ant-cleaved caspase-3 (Asp175) (CST, #9661) used in Western blotting has been verified in Pradella D, et al. Nature Communication, 2021 and Karki R, et al. Cell, 2021.
The rabbit anti-caspase-3 (CST, #9662) used in Western blotting has been verified in Wang XH, et al. Sci Rep, 2021 and Mulcahy ME, et al. Front Immunol, 2020.
The mouse anti-β-actin (Abcam, #ab8226) used in Western blotting has been verified in Jin P, et al. Gene, 2021 and Noback M, et al. Neurosci Lett, 2021.

Animals and other research organisms

Policy information about studies involving animals; ARRIVE guidelines recommended for reporting animal research, and Sex and Gender in Research

Laboratory animals

Both female and male mice aged 5-7 weeks were used for in vivo surgery and two-photon imaging, while mice aged 5-7 days were employed for acute brain slices experiments. Mice are family-housed with no more than 5 per cage, in a temperature between 21°C and 23°C and humidity between 55% and 60% room with a 12-12 hrs light-dark cycle. C57BL6/J mice (The Jackson Laboratory, IMSR_JAX: 000664) are breed in the animal facility at Chinese Institute for Brain Research (CIBR). Pannexin 1 conditional knockout mice (Panx1flox/+, GemPharmatech, Strain NO. T008074) with 140bp deletion in exon 2 are purchased from GemPharmatech, and homozygous mice are obtained for experiments. GFAP-cre-ERT2 mice (MMRRC, Stock#016992-MU) are originally obtained from MMRRC and are kindly provided by Dr. Wooping Ge's lab at CIBR. The LSL-Cas9-IRES-tdtomato transgenic mice (GemPharmatech, Strain NO. T002249) are generated by GemPharmatech and are kindly provided by Dr. Yulong Li's lab at Peking University. Cx3cr1GFP/+ mice (The Jackson Laboratory, IMSR_JAX: 005582) are originally purchased from Jackson Laboratory.

Wild animals

No wild animals are used in the study.

Reporting on sex	Except the MCAO model, both female and male mice are used in the experiments and data are plotted without discriminating the sex. For MCAO model, only male mice are used to avoid the influence from hormone cycles (see references: doi:10.1038/ jcbfm.2009.5 and doi:10.1097/00004647-200004000-00001). All these information is clearly written in the Method section of the manuscript.
Field-collected samples	No field-collected samples are used in the study.
Ethics oversight	All animal surgery and experimentation procedures are performed according to protocols approved by the Animal Care & Use Committees of the Chinese Institute for Brain Research (#CIBR-IACUC 007).

Note that full information on the approval of the study protocol must also be provided in the manuscript.

Plants

Seed stocks	*Report on the source of all seed stocks or other plant material used. If applicable, state the seed stock centre and catalogue number. If plant specimens were collected from the field, describe the collection location, date and sampling procedures.*
Novel plant genotypes	*Describe the methods by which all novel plant genotypes were produced. This includes those generated by transgenic approaches, gene editing, chemical/radiation-based mutagenesis and hybridization. For transgenic lines, describe the transformation method, the number of independent lines analyzed and the generation upon which experiments were performed. For gene-edited lines, describe the editor used, the endogenous sequence targeted for editing, the targeting guide RNA sequence (if applicable) and how the editor was applied.*
Authentication	*Describe any authentication procedures for each seed stock used or novel genotype generated. Describe any experiments used to assess the effect of a mutation and, where applicable, how potential secondary effects (e.g. second site T-DNA insertions, mosiacism, off-target gene editing) were examined.*